Nuclear Instruments and Methods in Physics Research A 666 (2012) 98–129

Contents lists available at SciVerse ScienceDirect

Nuclear Instruments and Methods in Physics Research A

journal homepage: www.elsevier.com/locate/nima

Review

Muon tracking and triggering with gaseous detectors and some applications

Archana Sharma

CERN, Geneva, Switzerland

ARTICLE INFO

Available online 9 December 2011

Keywords:
LHC
Muon
Gaseous detectors
MWPC
GEM
Triple-GEM
Forward
Endcap
High rate
Tracking
Triggering
Micropattern
Micromegas
ATLAS
CMS
ALICE
LHCb
Ageing

ABSTRACT

In this review paper the present state-of-the-art of muon detection systems using gaseous detectors at the Large Hadron collider (LHC) is described. Beginning with a discussion of the concepts of muon detection systems, a comparison of the various technologies used is made with respect to the challenges at present experiments, and developments for future upgrades are discussed. Starting from wire chambers, micropattern detectors are described and their readiness for upgrades is highlighted. Aging, long-term sustained operation and factors affecting gas choice are discussed. Finally some applications outside particle physics are also presented.

Contents

E-mail address: Archana.Sharma@cern.ch

0168-9002/$ - see front matter © 2011 Elsevier B.V. All rights reserved.
doi:10.1016/j.nima.2011.12.001

1. Introduction

The challenging and hostile scenario for muon detection at collider machines like the LHC [1], its upgrades and the future Linear Collider [2] has given rise to extremely innovative designs and exploitation of gaseous detectors for tracking and triggering. Nevertheless, the technologies exploited at the currently operational experiments at LHC are over a decade old due to the time and schedule constraints of construction and commissioning, large systems which can easily extend to the order of several thousand square meters and a construction time of several years. New detector technologies are being prototyped and evaluated for the LHC upgrades [3] and the ILC [4] for which the challenges for precision and radiation tolerance are ever more increasing. One of the most important goals at the LHC is the study of the Higgs sector of the Standard Model, the still undiscovered Higgs Boson, in a large range of mass would decay in the gold plated four muons final state, and be sensitive to compositeness at a higher energy scale. This requires a meticulous detection system to reconstruct the final muon states with a precision of for example $\approx 1\%$ for 1 TeV muon at LHC. Muons are identified with high accuracy due to the fact that they can penetrate through large amounts of material without any strong interaction, they have long lifetime hence offering lepton decay channels for heavy objects like $\tau \to \mu\mu$, $W \to \mu\nu$, $Z \to \mu\mu$, $t \to bw \to \mu\mu$.

Many channels for discovery physics contain muons in the final states (Fig. 1). The detection of muons at LHC consists of two major steps: the identification and measurement of muon parameters. The detectors require muon tracking and identification in an environment which is dense due to hadronic jets, in addition to low energy protons, photons and a neutron induced background [5]. The detectors at LHC have been optimized in their design to trigger on and reconstruct muons at a center of mass energy of 14 TeV and the highest luminosity at LHC namely $10^{34}\ \mathrm{cm}^{-2}\ \mathrm{s}^{-1}$. In addition to high energy muons (≈ 1 TeV) high efficiency and momentum resolution at low and intermediate energy are also required for most of the physics goals. Fast detectors with bunch crossing identification capability and good point resolution are hence, imperative.

1.1. Identifying muons

A direct manner of identifying the muon is to compare the measurements of the particle with known values of mass, charge, lifetime and decay modes. For lower energies ($\approx$ few GeV) a typical method is to measure the momentum and velocity of the particle

$$m = p(\beta^{-1} - 1)^{1/2} \tag{1}$$

where m and p are respectively its mass and momentum, and $\beta = v/c$, v being the velocity of the incoming muon. Combined with time-of-flight [6], Cerenkov and Transition Radiation detectors [7] the muon velocity may be inferred.

For higher energy muons i.e. above a few GeV up to the TeV scale, muon identification is based on the low rate of interaction of muons with matter. If a charged particle penetrates a large amount of matter (absorber) with minor energy losses and small angular displacement, it is considered to be a high energy muon. The large amount of absorber is typically 10 s of meters of insensitive material interspersed with sensitive detectors which can measure the properties of the particle. In a magnetic field the

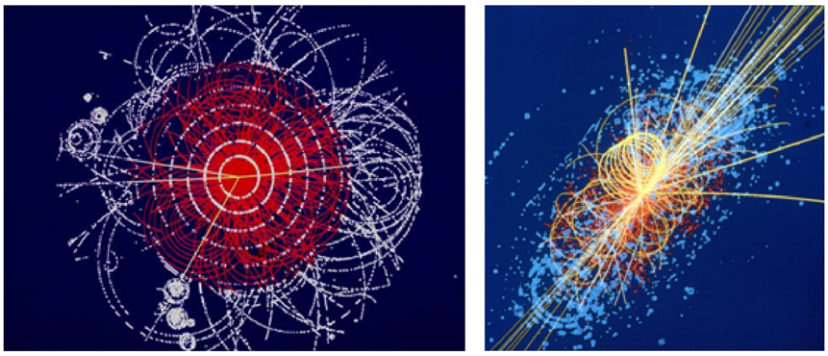

Fig. 1. Simulation of Higgs decaying into four-muons in ATLAS (left) and CMS (right) muon systems, the 'Gold plated' discovery decay mode: the guiding principle of the ATLAS and CMS muon systems.

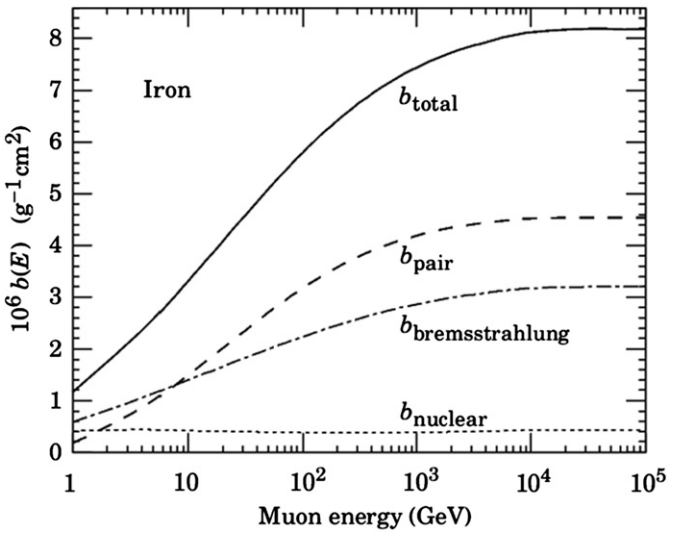

Fig. 2. In this figure is shown the typical muon energy loss in iron as a function of its energy, where b_{total} is the total energy while b_{pair}, $b_{bremsstrahlung}$, $b_{nuclear}$ represent the energy loss due to that interaction. Below $\approx$200 GeV these losses are primarily due to ionization. The average loss is about 2 MeV/g cm^2 equivalent to 1.4 GeV/m of steel. dE/dx energy loss curves describe the average energy losses; while numerous ionization collisions with very small energy transfers produce a localized trail of ionization that can be exploited by charged particle detectors to obtain the muon trajectory. The Landau's theory of ionization loss describes the fluctuations of these energy transfer collisions about the most probable value of the Landau distribution and are $\approx$20%.

particle trajectory is bent, and measuring the sagitta of bending by measuring several points on the trajectory, offers a clean method of momentum measurement exploited at the LHC experiments. The muon lifetime is about 2.2 μs and hence its decay paths for muons of 1 GeV, 10 GeV and 100 GeV are 7, 70 and 700 km respectively: for the applications at collider experiment muon systems the muons can be considered as stable particles. The absorbers with passage through matter, a muon loses energy (Fig. 2)[1] by electromagnetic interactions like ionizations, pair production (b_{pair}), Brehmsstrahlung $b_{bremsstrahlung}$ and photo nuclear interactions ($b_{nuclear}$). An excellent review of muon energy losses may be found in Ref. [8].

The high energy tail of the Landau distribution corresponds to stochastic collisions with large energy transfers resulting in knock on electrons: muons with energies above $\approx$0.2 TeV behave similarly to the electron creating electromagnetic shower cascades along their trajectory. Fig. 3 shows the momentum distribution of 1 TeV/c muons after traversing 3 m of iron, as obtained with the MARS14 Monte Carlo code [9] with the low energy radiative tail.[2]

A muon changes its direction due to electromagnetic interactions described by Eq. (2):

$$\sigma_\theta = \frac{(14\ \mathrm{MeV}/c)(L/Lrad)^{1/2}}{p} \tag{2}$$

where θ is a plane angle defined in Fig. 4. And L, and $Lrad$ are the length traversed by the muon and the radiation length of the material.

We obtain a good approximation with the above formula as an example, when a 50 GeV/c muon passes a 2 m block of steel with $Lrad$=1.76 cm the θ_y plane = 0.6 cm where θ_y plane is the angle of emergence of the muon. Several Monte Carlo and more complex calculations are used for high accuracy simulations.

[1] Taken from pdg, reproduced with permission.
[2] http://pdg.lbl.gov/2008/AtomicNuclearProperties/adndt.pdf.

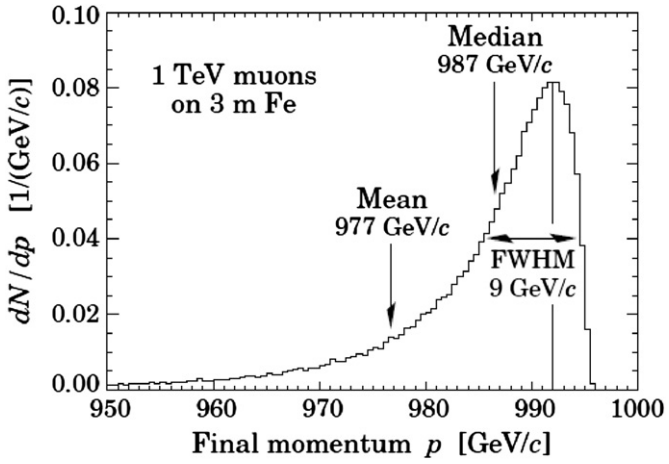

Fig. 3. Momentum distribution of 1 TeV/c muons after traversing 3 m of iron, as obtained with the MARS14 Monte Carlo code [9].

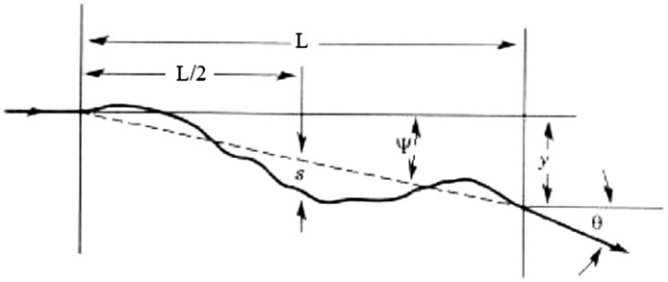

Fig. 4. Change of muon direction due to electromagnetic scattering.

Multiple Coulomb scattering is important since the contribution toward the final momentum resolution of a spectrometer will depend on the amount of absorber material present before the detector. And the point resolution of the detector is useful only when it is much less than the contribution from multiple scattering. Historically, there exist several simulation codes and packages for muon propagation in matter. The MUM code [9] is known for accuracy of simulation and speed. The PROPMU code [9] includes muon multiple scattering which MUM does not; where accuracy over small distances and muon multiple scattering potentially become more important, GEANT, FLUKA AND PROPMU have been compared here [10] with a few important differences in the sampling of e.m. interactions and energy-loss calculations. More recently the MARS has become the simulation package of choice for these simulations [9,10].

1.2. Reconstruction and muon momentum determination

Muon detection capability needs to extends over a large geometrical acceptance and the momentum resolution should be as best as, possible namely 1–2%.

In Fig. 5 a typical muon detector layout is shown schematically. If the absorber is too thin, then hadronic showers due to strong interactions of hadrons with the absorbers, can leak through with charged particles being detected after the absorber. These particle can then fake muon signals. Monte Carlo calculations and test beam measurements are typically employed to estimate the punch-through probabilities. Detectors have to be placed before and after an absorber such that punch-through rates due to hadron showers can be minimized. In addition to tracking, momentum measurements are made before and after the absorber and timing measurements are performed.

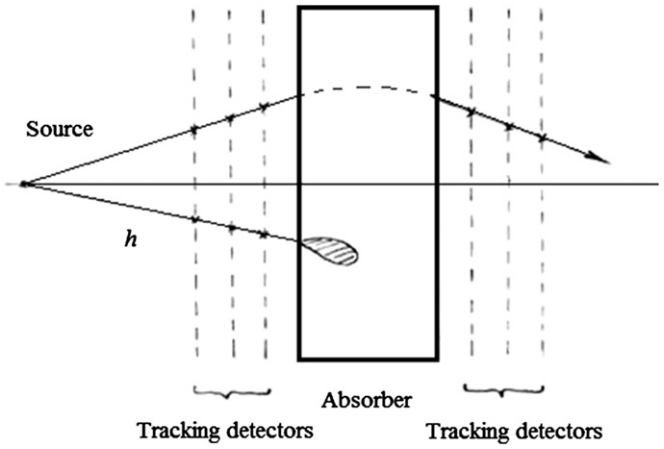

Fig. 5. Hadronic showers in absorbers.

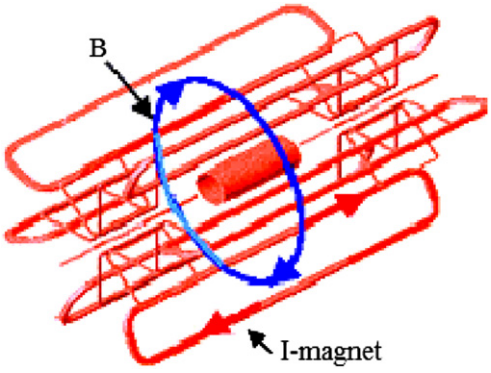

Fig. 6. A schematic view of a toroid and toroidal field.

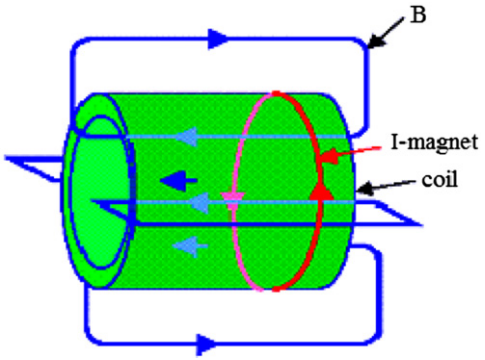

Fig. 7. In CMS the muon detector coverage is $|\eta| < 2.4$ with a magnetic field of 4 T [13].

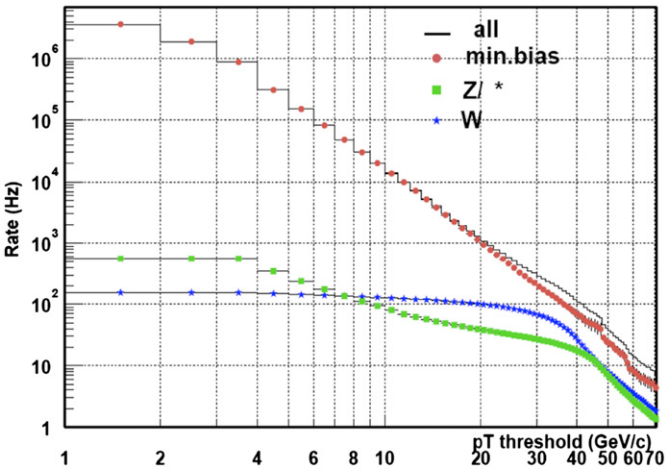

Fig. 8. The single muon rate at $L=10^{34}\,\mathrm{cm}^{-2}\,\mathrm{s}^{-1}$ vs p_T threshold.

At energies above ≈ 0.5 TeV, muons start losing energy due to radiation (γ, e^+e^-) with the result that a muon track is then accompanied by electromagnetic showers which subsequently results in high occupancy of tracking detectors; the requirements hence of very fast and multi-hit detectors and electronics. An increase in the number of planes of electronics and increasing the air gap between the absorber and the tracking detector are also other ways of reducing the electromagnetic background.

The muon can be bent inside a magnetized absorber, typically iron and steel which can be easily magnetized up to high magnetic fields.

The measurement of the momentum of incoming muon is limited by multiple scattering and the accuracy of the tracking detectors; a simplified expression for the relative momentum resolution σ_p/p for muons is the following formula:

$$\sigma_p \approx \frac{1}{B\cdot L}\left\{\left(14\ \mathrm{MeV}\sqrt{\frac{L}{L_{rad}}}\right)^2+\left(p\cdot\frac{2\sigma_x}{a}\right)^2\right\} \tag{3}$$

where L is the thickness of the material, L_{rad} the radiation length and σ_x the space resolution. Multiple scattering dominates the muon momentum resolution until about 100 GeV and the accuracy of the tracking detectors takes over at higher momenta. The momentum resolution may be improved by a reduction in multiple scattering. This can be done by bending the muon in air, not in iron after the tracker as in fixed target experiments, in the central tracker and in large air-core magnets as is done in ATLAS at LHC [11]. The intrinsic accuracy of the tracking detectors and an increase in the lever arm of the muon measurement also contributes to the improvement of the muon momentum resolution.

1.3. Instrumentation for muon measurements

The physics goals of experiments dictate much of the design considerations to detect the directions and momenta of low and high energy muons, which will provide a robust and precise physics signature for many physics channels. A trigger with muons in a hadron environment is a clean signature for basically all discovery physics. At LHC and beyond the rates from jets are huge and punch-through and feed-through dominates the rates. The punch-through imposes some pattern recognition demanding high granularity, while feed-through imposes good p_T resolution. Above the critical energy muon Brehmstrahlung is a challenge. Hence fast detection and fast trigger logic with good p_T assignment at the trigger level is the basic requirement. In addition, complete geometrical coverage as far as possible is critical, tracking and trigger capabilities with muon energies over 5–10 GeV are imperative; in turn requesting a fast detector with excellent timing resolution. All these considerations impose serious technological choices for the muon systems in the design of the experiment. The muon momentum is measured using sensitive detectors to measure the component transverse to the magnetic field

$$p_T = qBR \Rightarrow p_T\,(\mathrm{GeV}) = 0.3BR\,(\mathrm{Tm}) \tag{4}$$

$$\frac{L}{2R} = \sin\left(\frac{\alpha}{2}\right) \approx \frac{\alpha}{2} \Rightarrow \alpha \approx \frac{0.3LB}{p_T} \tag{5}$$

$$s = R\left(1-\cos\left(\frac{\alpha}{2}\right)\right) \approx R\frac{\alpha^2}{8} \approx \frac{qL^2B}{p_T} \tag{6}$$

where p_T,q,B are transverse momentum, charge of electron, magnetic field strength, respectively, and R and L are the radius of curvature and length (lever arm) of the magnet and α the angle in the plane perpendicular to B. The sagitta s is the deviation of the trajectory from a straight line defined by the entrance and exit positions in the field, x_1 and x_3. The position resolution σ_x for each layer of detector is given as follows:

$$s = x_2 - \frac{x_1 + x_3}{2} \tag{7}$$

$$\frac{\sigma(p_T)}{p_T} = \frac{\sigma(s)}{s} = \frac{\sqrt[2]{\frac{3}{2}\sigma(x)}}{s}. \tag{8}$$

Momentum resolution hence depends only on magnetic field B, lever arm L and σ_x, and not on radius, R. Another challenge is the hostile radiation environment which leads to two issues: rate capability and aging. They are discussed in detail in Section 2. These challenges are important to be met for the overall performance of the muon detectors especially for trigger with high rate capability. Redundancy is essential especially if achieved through independent and different detection systems.

1.4. Magnet

Since muon detection covers a large psuedorapidity range, there are two basic configurations of magnetic fields employed—a toroid which has field lines around the beam axis, and a solenoid which has field lines parallel to the beam concepts, have been exploited respectively by ATLAS [12] and CMS [13] experiments. The basic considerations have been driven for maximizing the lever arm of the measurement: BL^2, B being the magnetic field and L the length of the muon trajectory. The CMS experiment is operating at a record magnetic field of 3.8 T, and ATLAS chose to maximize L, hence it is the larger detector. The choice of absorber in a muon system is critical in order to reduce multiple scattering and hadron on punch-through. The most common absorber used is iron/steel [9] due to its low cost, high density hence compactness, and can easily be magnetized; concrete is also used. A large solid angle coverage can be achieved with toroids, the bending power of the magnetic field increases as $B.dl \approx \sin^{-1}(\theta)$; where θ is the production angle of the charged particle in question. Hence it compensates the increase of the momentum of the forward particles and yields a constant momentum resolution independent of pseudorapidity.

As shown in Fig. 6 the field lines of a toroid are completely immersed in the coils thus complicating the instrumentation, although reducing the stray fields. A large number of coils are required to keep the field uniform. The coils have to be large and mechanical supports extremely rigid, hence a toroid solution is excellent if magnetic field needs to be kept small. On the other hand a solenoid (see schematic in Fig. 7) offers the advantage that the track bending takes place in the transverse plane and a precise knowledge of interaction point can therefore be used in the trigger and for momentum determination.

Due to their mechanical stability, the circular coils afford a higher magnetic field facilitating the first level trigger due to the resultant larger bending. The iron return yoke acts as a muon filter and facilitates a repetitive muon momentum measurement. A strong central field allows the size of the entire detector to be reduced but then the tracking and triggering chambers must be operated in this field. An optimized muon momentum is achievable with a combination of different detector concepts open air-core magnet in combination with or without an iron absorber.

Table 1
Rates at CMS and ATLAS muon trigger.

Parameter	LHC	HL-LHC
s	14 TeV	14 TeV
L	10^{34}/cm^2 s	10^{35}/cm^2 s
Bunch spacing	25 ns	12.5 ns
Interactions/crossing	≈ 12	≈ 62
$dN/d\eta$ crossing	75	375
CMS particle flux 1st muon layer $\eta \approx 2.4$	≈ 1 kHz/cm^2	≈ 10 kHz/cm^2
CMS particle flux 1st muon layer $\eta \approx 2.4$	≈ 1 kHz/cm^2	≈ 10 kHz/cm^2
ATLAS particle flux 1st muon layer $\eta \approx 2.4$	$\approx 1-10$ kHz/cm^2	$\approx 1-15$ kHz/cm^2
ATLAS particle flux 1st muon layer $\eta \approx 2.4$	$\approx 1-10$ kHz/cm^2	$\approx 1-15$ kHz/cm^2

2. Radiation environment

2.1. Particle rates and trigger

The inclusive rate of prompt muons and multimuons at LHC have been extensively calculated [14] and measured [10]. Prompt muons come from the decays of heavy flavors (c,b,t quarks) and are 'isolated' from those coming from W and Z-decays. Since these muons come usually constrained in jets they can be identified and can provide the trigger. In a hadron machine, physics processes are characterized by jets, but discrimination of signal events can be provided by the muons in the final state that can used as

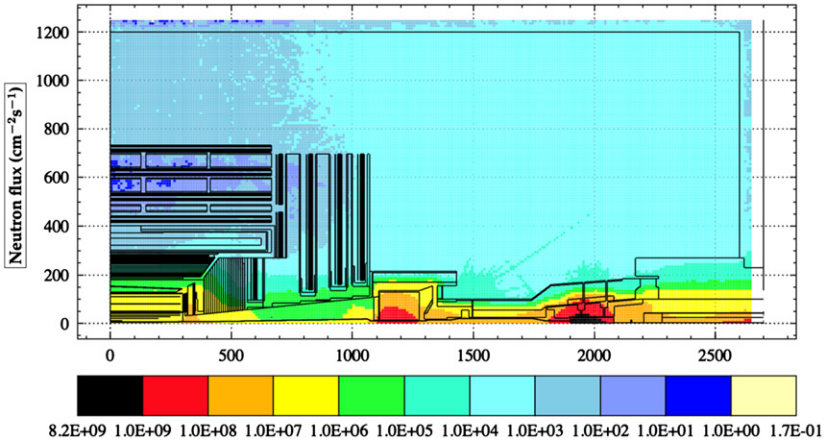

Fig. 9. Radiation map showing the distribution of the absorbed dose in various subdetectors at CMS [14].

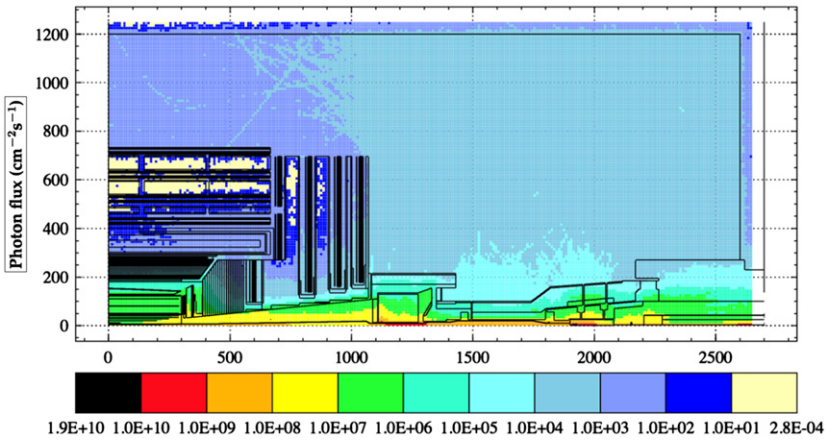

Fig. 10. Radiation map showing the distribution of the absorbed dose in various subdetectors at CMS [14].

Table 2
Comparison between CMS and ATLAS muon trigger.

ATLAS	CMS
Main magnet Toroid, $B=0.7$ T	One magnet Solenoid $B=4$ T
Homogeneous B-field	Inhomogeneous field at large η
Straight track in (r,ϕ)	Extrapolation to z-coord. of the beam (cm)
Tracker extrapolation to beam, additional solenoid, $B=2$ T	Trigger on high momentum muons; impact parameter
Bending in (r,z)	In (r,z) straight track
No iron in muon system	Requires return yoke in muon system

trigger signature. At LHC for example, the total inelastic cross-section is ≈ 100 mb while the interesting physics signal is characterized by cross-sections typically ≈ 1 pb, with $\approx 10^9$ interactions/s and in a background of 10^{11} particles/s, a Higgs for example would give a detectable signal per 10^{14} events at LHC at design luminosity. In Fig. 8 is shown the single muon rate at design luminosity LHC versus p_T threshold [15].

The radiation doses in the central region are practically independent of center of mass energy and a linear function of luminosity. Doses especially from accelerator related backgrounds and neutrons have to be carefully estimated since high energy muons start to irradiate γ (e.m. showers) and lose more energy due to radiation losses than due to ionization at a few hundred GeV creating backgrounds in the muon tracking detectors and requires corrections for momentum measurements. Typical doses for muon detectors at LHC and its upgrades is 1–2 Mrad per year depending on the experimental conditions [14], a good p_T resolution is required at the trigger level to avoid a large feed-through from low p_T muons.

2.2. Rates of expected muons

A comparison of the rates for muons expected at LHC, HL-LHC (High Luminosity LHC) and ILC is reported in Table 1 [17].

At these rates, an optimal trigger system needs to select the important physics processes which have been estimated with a margin of a safety factor of 3, and achieve a rejection factor of nearly 10^7. Since sequential selection criteria are used at LHC, the trigger systems have well-defined levels to cope with these rates. Fast detectors are used to provide triggering information and sometimes several precision detector systems participate in the trigger decision; redundancy is essential to provide a robust and flexible muon trigger.

Table 3
A comparison of typical coverage and performance parameters for muon detectors in ATLAS [12] and CMS [13].

Muon chamber	ATLAS	CMS
Drift tubes	MDTs	DT s
Coverage	$\lvert\eta\rvert < 2.0$	$\lvert\eta\rvert < 1.2$
Number of chambers	1170	
Number of channels	354,000	
Function precision measurement		
Cathode Strip Chambers		
Coverage	$2.0 < \lvert\eta\rvert < 2.7$	$1.2 < \lvert\eta\rvert < 2.4$
Number of chambers	32	468
Number of channels	31,000	500,000
Function	Precision measurement	Precision measurement, triggering
Resistive Plate Chambers		
Coverage	$\lvert\eta\rvert < 1.05$	$\lvert\eta\rvert < 2.1$
Number of chambers	1112	912
Number of channels	374,000	160,000
Function	Triggering, second coordinate	Triggering
Thin gap chambers		
Coverage	$1.05 < \lvert\eta\rvert < 2.4$	–
Number of chambers	1578	–
Number of channels	322,000	–
Function	Triggering, second coordinate	–

2.3. Radiation environment

As mentioned above, muon chambers are situated a few meters away from the interaction point. The radiation doses that muon chambers typically seen in colliding experiments like the LHC are $\sim$ Mrad per 10 years of operation as shown in Fig. 9 [14].

Photon fluence in the central region of the CMS detector for example, after 100 fb^{-1} luminosity may be seen in Fig. 10, calculated for 14 TeV pp collisions [14].

It can be seen that a typical rate of 10^{14} neutrons/cm^2 may be expected in muon tracking detectors. In Table 1 the rates of muon at LHC and HL-LHC are shown. These numbers are relevant in the context of long term and sustained operation of the detectors as will be explained in Section 6.

3. Gaseous detectors for muon chambers at LHC

The muon system in most modern HEP experiments is based on large area gaseous detectors which can be large covering up to

several thousands of meter square. The muon systems layout of ATLAS and CMS as examples are shown in Figs. 12 and 14 the chambers are typically categorized into two sets: one for dedicated precision measurement of muon tracks and the second set dedicated for defining a muon trigger. The basic principle of muon measurement is to obtain at least three points along the muon trajectory since multiple scattering also plays a role hence this measurements can be improved by combining trajectory with momentum measurement of inner detection typically high precision of order of 80 μm that have been achieved in both ATLAS and CMS. A contribution toward this resolution also comes from the role of a strong magnetic field and an excellent knowledge of magnetic field map. The main design parameters of the two muon systems are summarized in Table 2.

The detectors used for the experiments at LHC are as varied as the concept and design of the individual experiment concept. In ATLAS there are four different types of gas detectors used, mainly dictated by the sensitive surface covered, trigger and precision and also importantly due to differing radiation environment. In the next sections we will review the different detector technologies used in different experiments with their advantages and disadvantages. In Table 3 are presented the typical eta coverages, chamber resolutions and the number of hits in the barrel and endcap regions of ATLAS (Figs. 11 and 12) and CMS (Figs. 13 and 14).

The quoted spatial resolution does not include chamber-alignment uncertainties which in itself is a subject of one of the articles in this volume. Similarly, for the intrinsic time resolution of each chamber type, contributions from signal propagation and electronics distributions need to be added.

3.1. Multi-wire proportional chambers and wireless chambers

Although the multi-wire proportional chamber has a long history of developments over the last few decades, the robustness

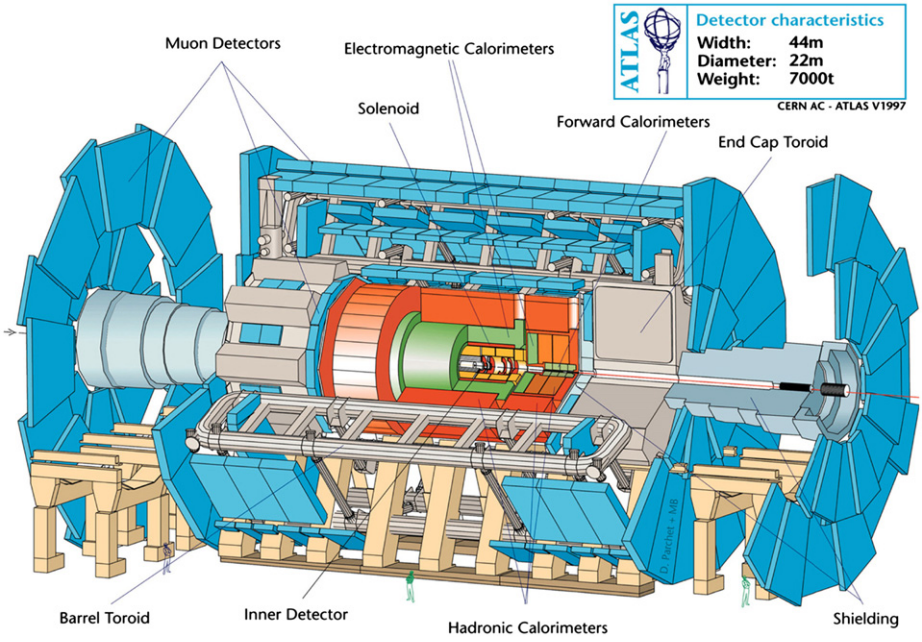

Fig. 11. The ATLAS MUON Spectrometer Muon spectrometer is the outer layer (in blue) of ATLAS detector (~22 m high and 44 m long); 5500 m^2 covered by muon detectors or 400,000 single drift tube detector, grouped in 1200 chambers. (For interpretation of the references to color in this figure legend, the reader is referred to the web version of this article.)

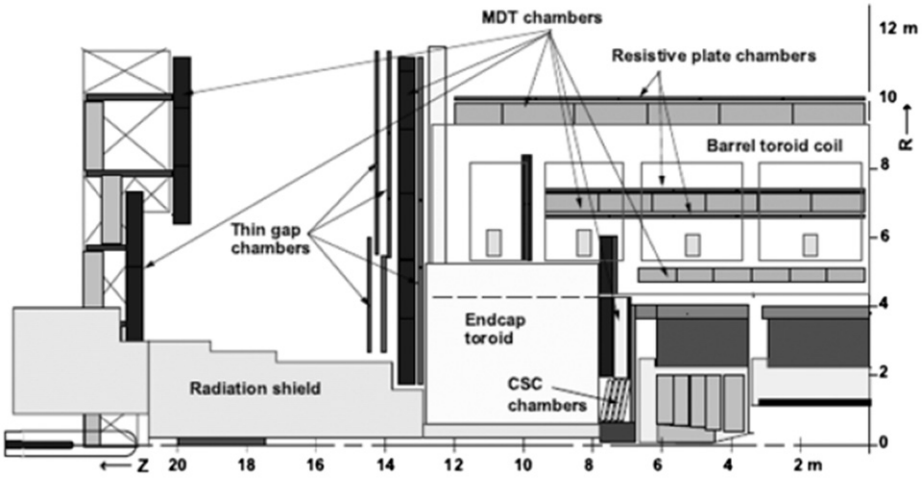

Fig. 12. Cross-section of the ATLAS muon system in a plane along the beam axis (bending plane). Infinite-momentum muons would propagate along straight trajectories and typically traverse three muon stations.

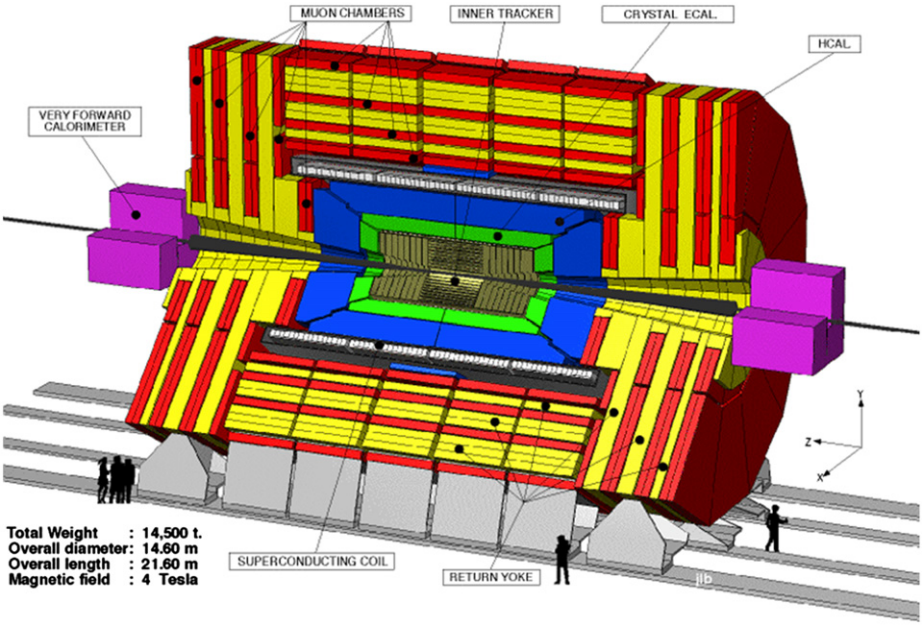

Fig. 13. The CMS detector. All in red is the muon system; yellow iron return yoke also seen are barrel and end caps of muon chambers. (For interpretation of the references to color in this figure legend, the reader is referred to the web version of this article.)

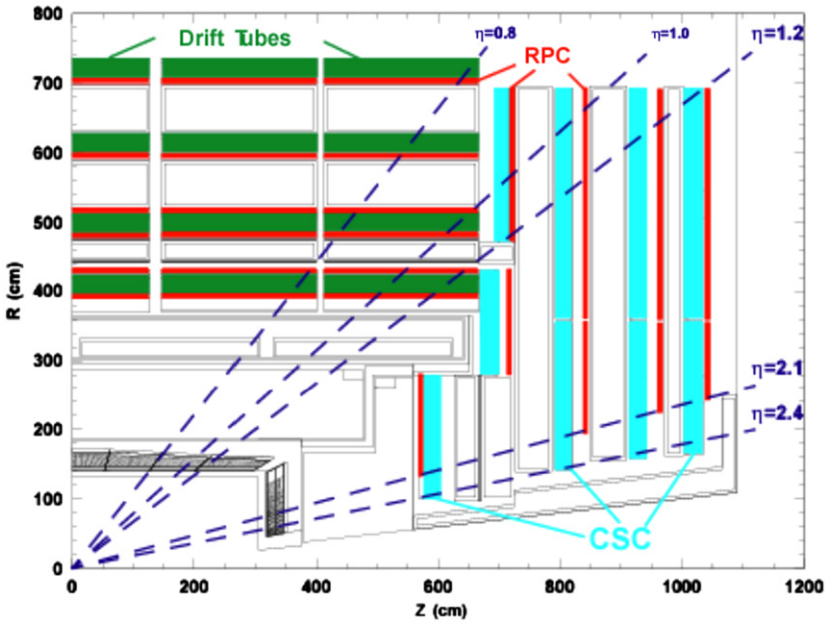

Fig. 14. Barrel and endcap muon chamber in CMS.

of this kind of detectors makes it the detector of choice for tracking and triggering in medium radiation environment at the LHC. They have been amply exploited at ATLAS [12], CMS [13], LHCb [16] and ALICE [18]. In ATLAS the central tracking detector namely the TRT [19] is made of single wire proportional tubes. Further MWPCs have been proposed for the International Linear Collider [2], and the Straw Tracker of the NA62 experiment [20]. Apart from wire chambers, a very successful 'wireless' technology—the Resistive Plate Chamber (RPC) has also been commonly used for cheap large area coverage for muon detection [12,13,21]. In the following we describe fast trigger detectors and differentiate these from high precision tacking chambers.

4. Detectors for trigger

In the following three sections we will describe detectors specifically designed to have a response time fast enough so that they can be used for triggering purposes.

4.1. Resistive Plate Chambers (RPC)

Resistive Plate Chambers (RPCs) are gaseous parallel-plate detectors that combine good spatial resolution with a time resolution appropriate for fast spacetime particle triggering. In one of the most popular versions, the electrodes are made out of

phenolic resin (bakelite) as introduced by Santonico [22], with a bulk resistivity of $10^{10}-10^{12}\ \Omega$ cm, separated by few millimeter of gas gap delimited by the bakelite surfaces which are coated on the outside surface, with conductive graphite paint to form the HV and ground electrodes respectively. The read-out is performed by means of aluminum strips separated from the graphite coating by an insulating PET film as shown in Fig. 15.

RPCs have been demonstrated to operate in streamer mode, i.e. the electric field inside the gap is kept high enough to generate limited avalanche multiplication localized near the crossing of the ionizing particle originally thought to be operating in streamer mode. However, the rate capability obtained in such operational conditions is limited (≈ 100 Hz/cm^2). A significant improvement was achieved by operating the detector in the so-called avalanche mode; the electric field across the gap and the gas amplification is reduced yet the lower gain in the avalanche mode is compensated by the use of signal amplification at the front-end level. The substantial reduction of the charge produced in the gap improves by more than one order of magnitude the rate capability (≈ 1 kHz/cm^2). A typical RPC is capable of tagging the time of an ionizing event in times of the order of few 10 ns, permitting bunch crossing identification at LHC, while using special techniques few nanoseconds of time resolutions have been demonstrated [23]. A fast dedicated muon trigger detector, based on RPCs, can therefore identify unambiguously the relevant bunch-crossing with which the muon tracks are associated, even in the presence of the high rate and background expected at LHC. Signals from such detectors directly provide the time and the position of a muon hit with the required accuracy.

At large experiments, Bakelite RPCs have been the detector of choice to cover thousands of meter squared of sensitive volume: a total of 15,000 m^2 for ATLAS and CMS combined. Some results from quality control during construction of the two systems are shown in Fig. 16. Performance of the large systems needs to be monitored constantly and for ATLAS and CMS may be seen in Fig. 17.

During the commissioning phase with cosmics the reconstructed muons in the ATLAS and CMS RPC system are shown in Fig. 18. In the ATLAS case the tracking is based on RPC space points, which are defined by orthogonal RPC cluster hits. The pattern recognition is seeded by a straight line defined by two space points belonging to the two middle planes. Space points not part of any previous track and inside a predefined distance from the straight line are associated to the pattern. Patterns with points in at least three out of four layers in middle planes are retained and a linear interpolation is performed in the two orthogonal views.

Gas system aspects are rather important and continuous online monitoring of the gas mixture is imperative along with environmental variables such as pressure, temperature and relative humidity as shown in Fig. 19 for CMS.

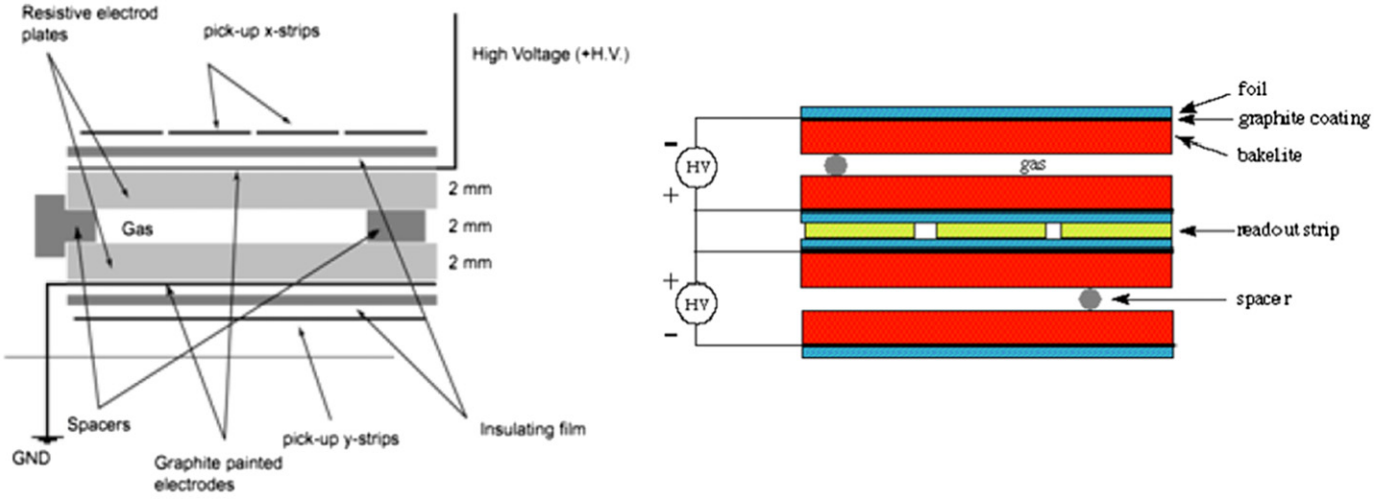

Fig. 15. Schematics of a Resistive Plate Chamber (RPC)—(left) Single gap RPC—schematic; (right) double Gap RPC used in CMS.

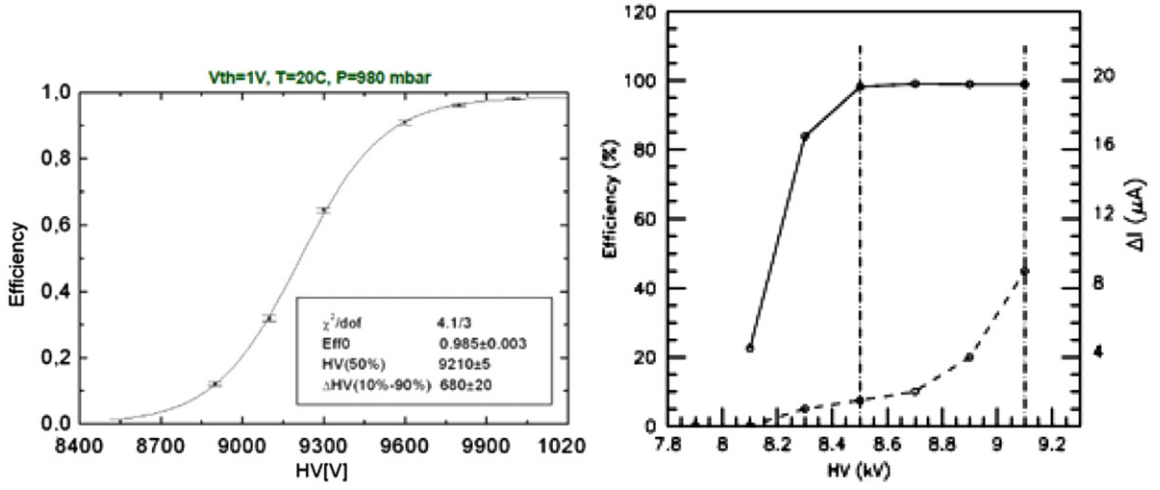

Fig. 16. Efficiency measurements from RPCs for ATLAS (left) and CMS (right) during commissioning phase.

4.2. Multigap RPCs

The multigap glass RPCs used for the ALICE time-of-flight system [25] have a time resolution ~ 50 ps as reported in Ref. [21]. The ALICE detector is optimized to investigate heavy ion collisions in which for identifying particles a time-of-flight (TOF) technique is used for the mid range of momenta (0.5–2.5 GeV/c) [26].

The TOF array based on the multigap Resistive Plate Chambers (MRPCs) shows an excellent performance in separating pions from kaons. The resistive plates are made out of thin

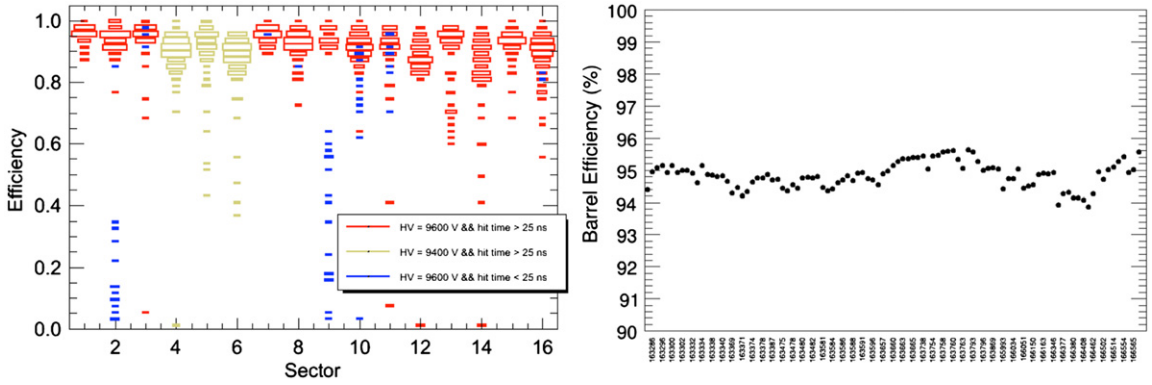

Fig. 17. On top left we see the performance of ATLAS RPCs and in top right the efficiency for CMS RPCs during operation phase.

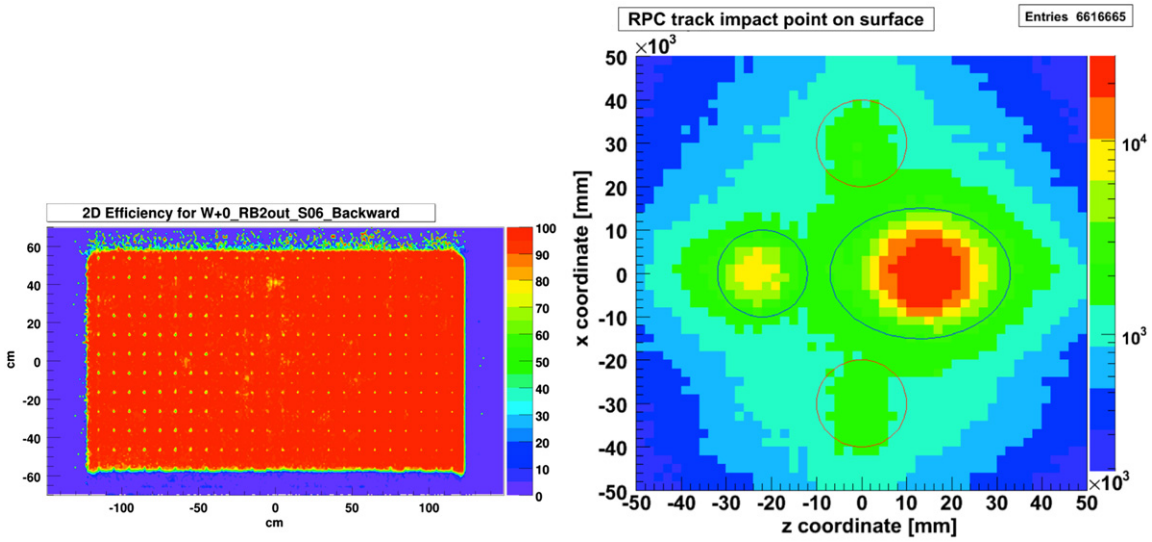

Fig. 18. (Left) Efficiency distribution in one of the wheels of the CMS barrel RPC system. (Right) ATLAS RPCs: cosmics muon map reconstructed by off-line RPC standalone muon monitoring projected on surface ($y=81$ m).

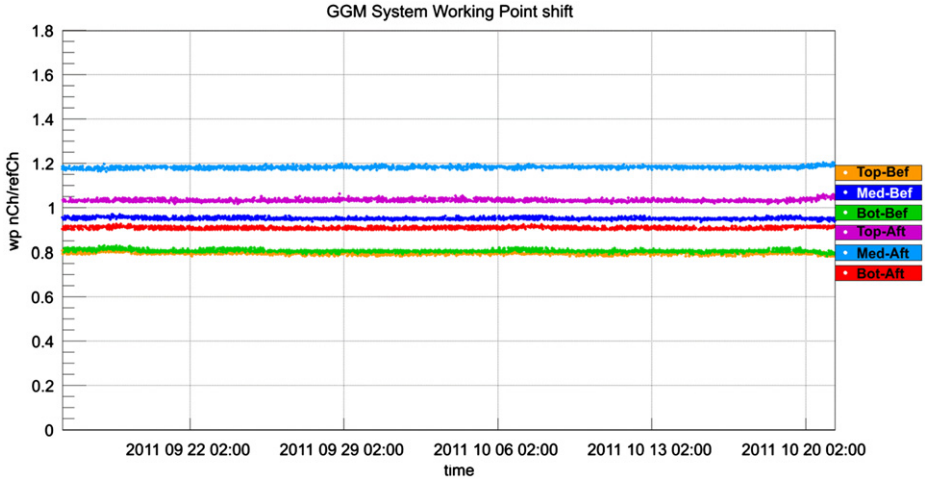

Fig. 19. RPC working point monitoring performed by the gas gain monitoring system at CMS gas building. The dependence on environmental variable is removed online in order to spot the presence of any gas contaminant [24].

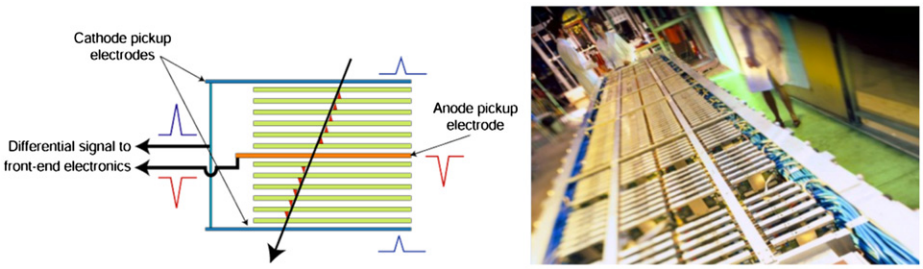

Fig. 20. (Left) Schematic of a multigap Resistive Plate Chamber; (right) large MRPC module under construction for the ALCE time-of-flight detector.

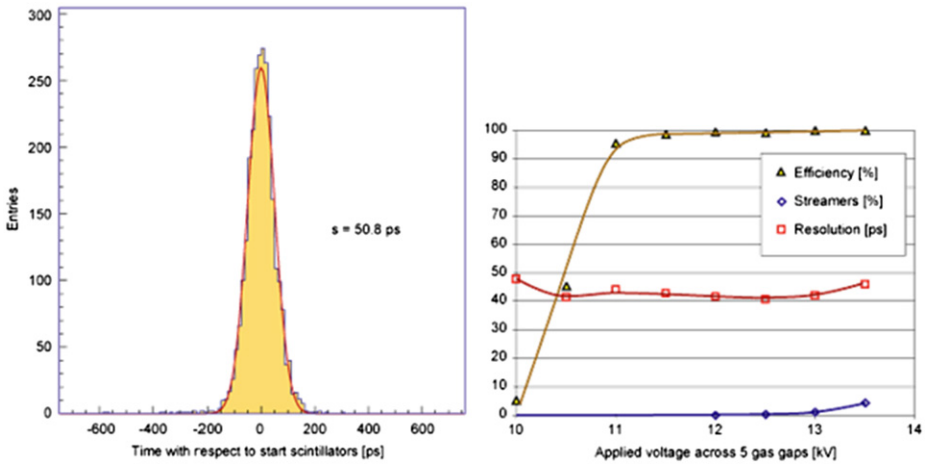

Fig. 21. Performance of a multigap Resistive Plate Chamber: time resolution and efficiency with fraction of streamers.

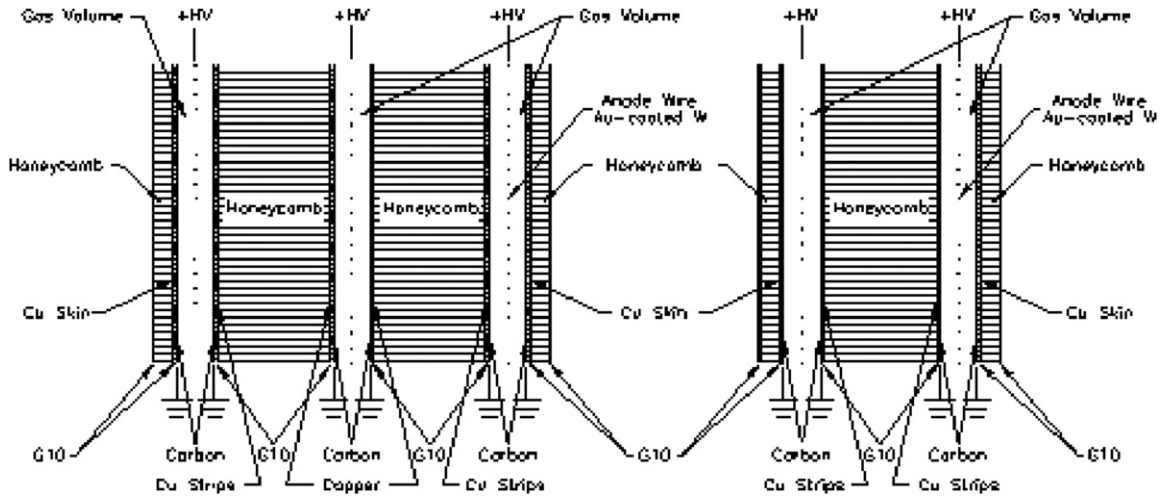

Fig. 22. Schematic of thin gap chambers.

(400−550 μm thick) sheets of 'soda-lime' glass and fishing line is used to create the 250 μm spacing between the sheets. The simplicity of the construction and the relatively low cost allowed the collaboration to build a very large area TOF (around 140 m^2) that covers the full ALICE barrel region, with ∼150 K read-out pads. The global time resolution achieved in Pb–Pb collisions at ALICE is 86 ps [21]. Glass RPC with special treatment may be used for very high rate applications and imaging [27]. In Fig. 20 are shown the schematics and some typical operational characteristics of these detectors while in Fig. 21 is shown time resolution and efficiency performance of the MRPCs [21]. The glass RPCs used for the ALICE TOF have a time resolution ∼50 ps as reported in Ref. [27] although these do not compete with Bakelite RPCs for the large areas like those covered in ATLAS and CMS detectors would be unaffordable.

4.3. Thin gap chambers TGCs

Thin gap chambers are used for triggering in ATLAS [12], as the name suggests they exploit a very small drift distance and a very close wire spacing which results in a time resolution of ∼25 ns, the penalty to pay is to use a heavily quenched and flammable gas like *n*-pentane with severe safety implications.

In Fig. 22 a schematic diagram of a thin gap chamber is shown, and in Fig. 23 some performance parameters are reported from Ref. [28].

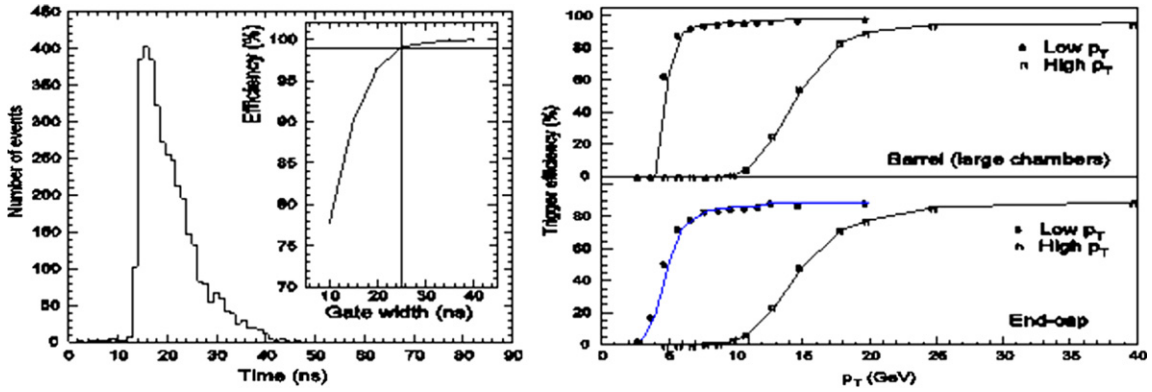

Fig. 23. Time resolution and efficiency for low and high p_T muons for ATLAS TGCs.

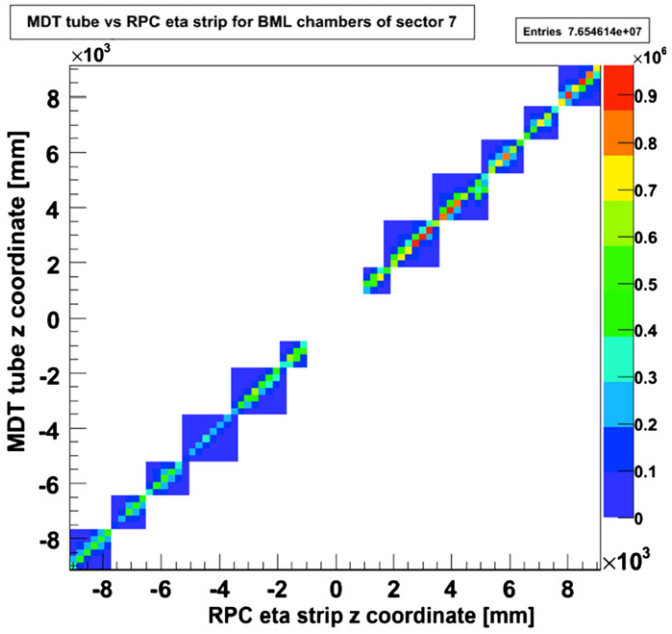

Fig. 24. Correlation between MDT tube hits and TGC tracks [28].

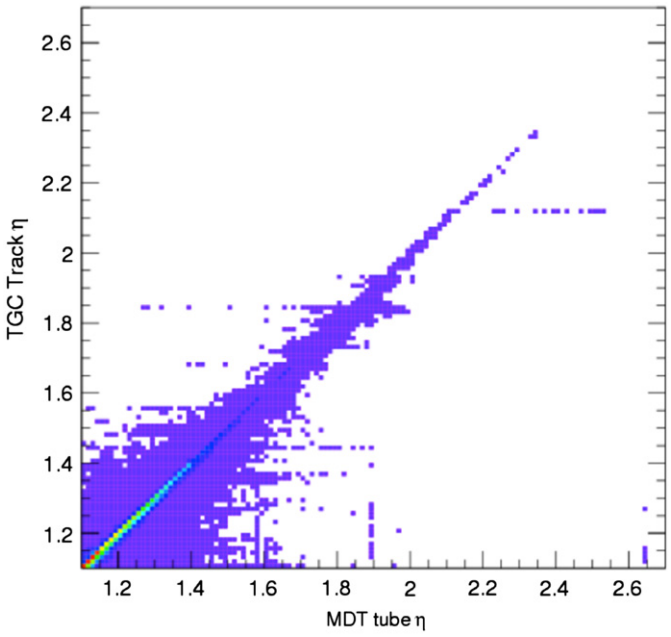

Fig. 25. Spatial correlation between MDT tubes and RPC η hits with cosmic data.

Independent muon systems may be used to find correlations between tracks coordinates and calibrations used to reject random hits. As an example in Figs. 24 and 25 correlations between MDT with RPC and TGC are shown. Further details may be found in Ref. [29].

5. High position resolution detectors

5.1. Precision drift tubes

A drift tube tracking detector in a large HEP experiment consists of an array of cells with an anode wire in the center; the sizes of these cells ranges between 1 and 10 cm^2, the total number of cells is of the order of 10^4–10^5 and individual chamber are up to 10 m long, consisting of 10^2–10^3 cells each. The basic scheme of such detector is shown in Fig. 26 the advantages are that if a wire is broken it is localized inside a single cell. The detector itself is made of simple repetitive cell with characteristics defined by an individual cell with cell walls creating the self-supporting detector elements.

In order to measure the muon track with high precision the electron drift time is measured and coordinates of the muon are extracted using the space-time relationships which can be accurately computed using sophisticated simulations program [30]. As shown in Fig. 26 resolutions below 100 μm have been routinely reached operating with a gas mixture of Ar/CO_2 at 3 bar taking advantage of the very low diffusion properties of this gas and the operational characteristics in a magnetic field—see Section 1.4.

The simple proportional chamber described above combined with a high precision alignment system [31] is exploited to the maximum by the ATLAS Muon System. It consists of two multilayers of monitored drift tubes (MDTs), see Fig. 27, separated with a spacer frame consisting of three cross-plates and two long-beams, in which the MDT optical alignment system is situated [32]. The MDT chambers in the middle and outer layers of the muon spectrometer have multilayers consisting of three MDT layers. Chambers in the inner stations have multilayers built of four MDT layers in order to optimize the pattern recognition performance at the high background rates close to the interaction point. Another arrangement of the wire chamber with anode and sense wires called 'drift tubes' has been exploited for muon tracking and momentum measurements in CMS (Fig. 30). The main features of drift tube cell are shown in Fig. 28 while Fig. 29 depicts the time resolution and efficiency.

The spatial resolution is dependent on fluctuations in primary ionization statistics, diffusion of drifting electrons, mechanical tolerances of wire precision and positioning ($\sim$50 μm), wire sag due to gravitation and subsequent inhomogeneity of electric

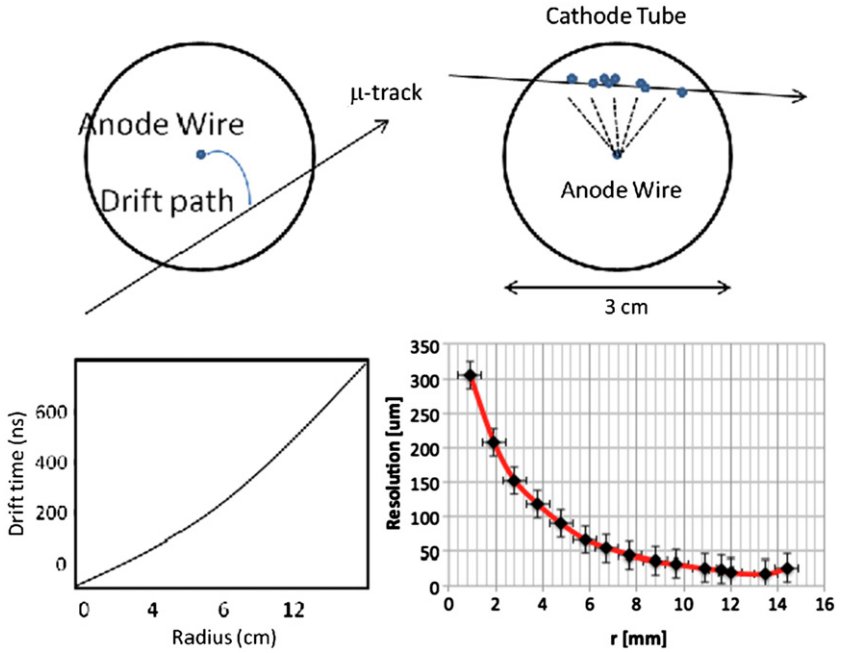

Fig. 26. With a radius of 1.5 cm, a gas mixture of Ar/CO_2 at 3 bar pressure, the space time relationship and results of resolution measurement for the ATLAS MDTs.

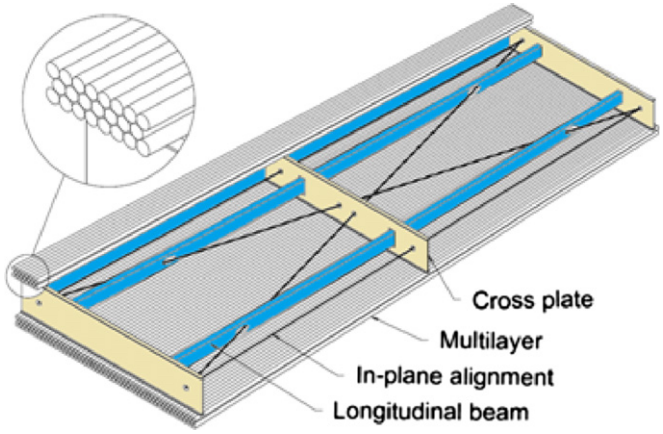

Fig. 27. A schematic view of an MDT chamber consisting of several individual tubes.

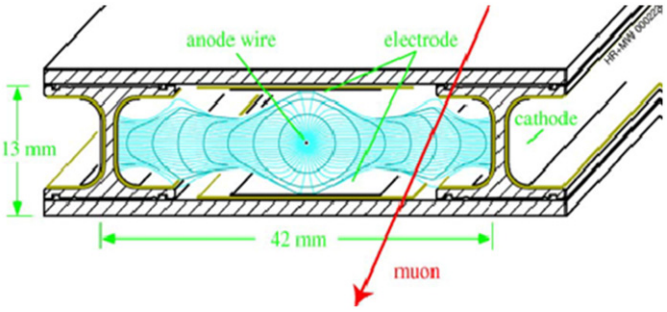

Fig. 28. The drift tube cell of CMS characterized by a nearly linear position drift time relation thanks to the introduction of additional potential wires or field shaping electrodes.

field, variations of drift velocity (e.g. due to gas impurities, gas purification) and temperature and pressure dependences. These effects will be discussed in details in Section 7.4.

Some advantages and disadvantages of these kind of wire chambers are reported in Table 4.

5.2. Cathode Strip Chamber (CSCs)

In addition to Resistive Plate Chambers, the CMS endcap also contains Cathode Strip Chambers (Fig. 31) with $\sim$0.5 M channels, while in ATLAS the CSCs are exploited only for high-η (Table 5).

Cathode Strip Chambers [13] (as shown Fig. 33) are exploited in the LHC experiments due to the robustness of large area of multiwire chambers with strip readout; it is a segmented cathode readout chamber made of conductive strips (Fig. 32). With several planes of wires and readout strips this detector provides a robust solution for operation in a magnetic field. At LHCb too, MWPCs form the muon system [16] with the anode wire planes centered in a 5 mm gas gap and consist of 30 mm diameter gold-plated tungsten wires [16] with 2 mm spacing.

5.3. Micro Pattern Gas Detectors (MPGDs)

The invention of the microstrip gas chamber (MSGC) in 1988 [33] marked a new era of high rate capable gaseous detectors called micropattern detectors [34]. An MSGC is composed of a pattern of thin anode and cathode strips on an insulating substrate with a pitch of a few hundred micrometers, see Fig. 34.

With a drift electrode delimiting the gas volume and with appropriate potentials applied, the electric field is such that positive ions are removed much faster from the avalanches, increasing rate capability by some two orders of magnitude in comparison with a multiwire proportional chamber. The COMPASS [35], TOTEM [36] and LHCb [37] experiments have used MPGDs in their tracking and triggering systems providing rich experience for upgrades of muon system in the present and future experiments.

The salient features of this kind of detector are a localization accuracy of $\sim$30 μm, double-track resolution of 400 μm and a good energy resolution (12–15%). Long-term and magnetic field operations have also been demonstrated. Advances in photolithography and the application of silicon foundry techniques heralded a new era in the design and fabrication of "micropattern detectors". The microdot (Fig. 35) chamber is the ultimate gaseous pixel device [38], with anode dots surrounded by cathode rings.

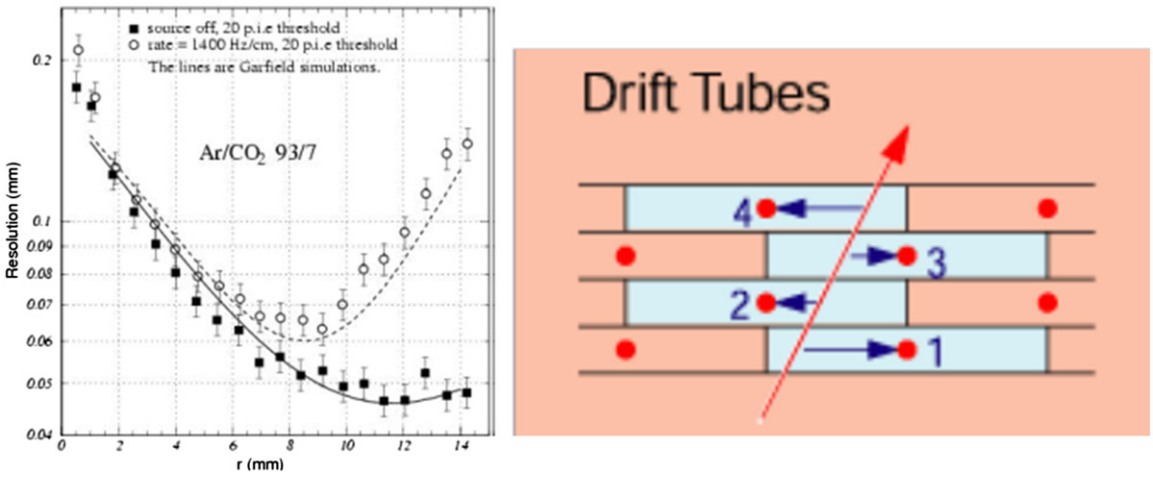

Fig. 29. Time resolution and efficiency for low and high p_T muons for ATLAS TGCs.

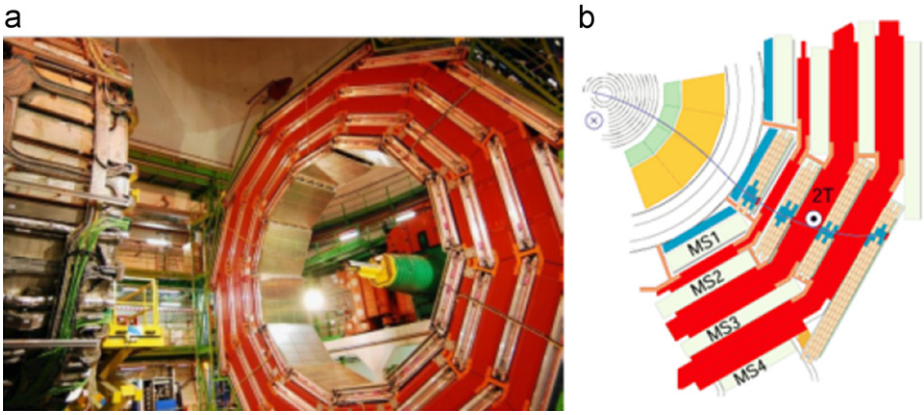

Fig. 30. (a) Drift tubes inserted in one of the wheels of CMS. The red part is the iron yoke of the CMS solenoid which houses the muon detectors; in (b) one can see the detector providing a muon measurement extending up to the interaction point with several points (blue) given from the four layers of drift tubes. (For interpretation of the references to color in this figure legend, the reader is referred to the web version of this article.)

Table 4
Some advantages and disadvantages of proportional tubes is given.

Advantages	Disadvantages
High intrinsic coordinate resolution ~ 0.5 mm easily achievable	Large number of thin wires (CMS-over 10^6 wires)
Small sensitivity to backgrounds	Need to purge the system with gas mixture
Density is low, small hydrogen concentration which translates into less neutron background	
High detection efficiency ~ 100 or more primary electron/ion pairs per mip-99.9% efficient	
Large signals	
Gas gains up to $\sim 10^5-10^6$	
Low intrinsic noise	
Rate capability	Inefficient zones
$\sim 10^6$ particles/cm^2 s	Near wires supports
Multi-hit capabilities in large drift cell	Near ends of the modules
Time resolution	Needs clean room assembly facility
Single layer $\sim$ max drift time	EXB Effects, deteriorated performance
Double layer $\sim$ a few ns	
	Ageing effects
Over two decades construction/operation experience	Gas impurities dependence
Possibility of dE/dx measurements	Wire failure can affect all chamber
Reasonable cost	

Although achieving gains of about 10^6, it does not discharge, probably because the field emulates the $1/r$ field of an anode wire. Detectors combining the techniques of silicon foundries and micro-photolithography have also been made namely the Gas-on-slimmed-silicon-pixels, GOSSIP [39] shown in Fig. 36, GOSSIP is a gaseous micro-pixel detector with a very thin drift gap intended for a high rate environment like at the pixel layers of ATLAS at the high luminosity LHC. The detector yields not only

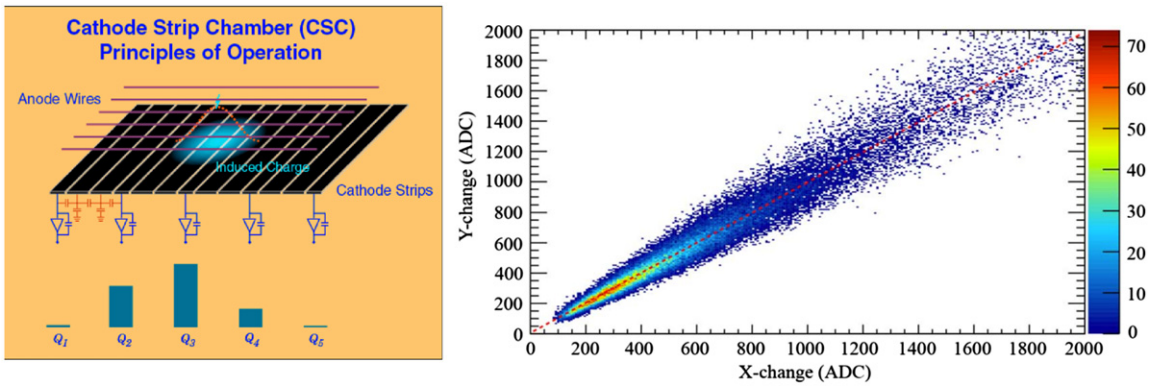

Fig. 31. Layout of the Cathode Strip Chamber, induced charge is measured by cathode strips, center of gravity gives the coordinate and the anode wire gives the second coordinate.

Table 5
Salient features of MPGDs.

Advantages	Disadvantages
High intrinsic coordinate resolution 0.1–0.2 mm	Smaller sectors for lowering discharge capacitance easily achievable, minimal inefficient zones
Small sensitivity to backgrounds	Need to purge the system with gas mixture
Density is very low, small H concentration	Possible gas leaks
Small EXB effect	
Better spatial resolution in a strong Magnetic field	Needs clean room assembly facility
Better two hit separation	
Capability to suppress Ion feed back	
High detection efficiency $\sim$100 or more primary electron/ion pairs per mip-99.9% efficient	
Large signals gas gains up to $\sim 10^4$	
Low intrinsic noise	High Rate Capability 10^6/mm^2 needs clean room assembly facility
Time resolution $\sim$ a few ns	
Operation in magnetic field proven	
Over one decade construction/operation experience	
Possibility of dE/dx measurements	
Reasonable cost	

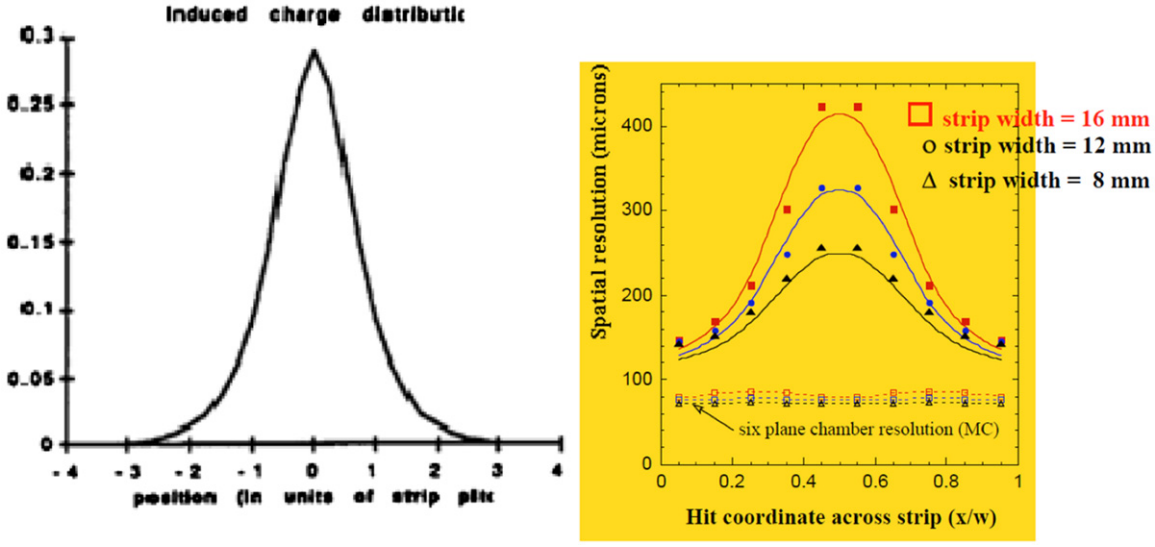

Fig. 32. Induced charge distribution on the cathode strips in a CSC chamber; varying strip widths.

the crossing point of a traversing minimum ionizing particle (MIP), but also the angle of the track, thus greatly simplifying track reconstruction. These high accuracy devices although not suitable for large area muon detection applications, for smaller areas ($\sim$ few m^2) they seem to be the detector of choice competing with solid state devices mainly due to cost.

A very asymmetric parallel plate chamber, the MICROMEGAS detector [40], takes advantage of the behavior of the Townsend

Fig. 33. Cathode Strip Chambers mounted on a CMS endcap.

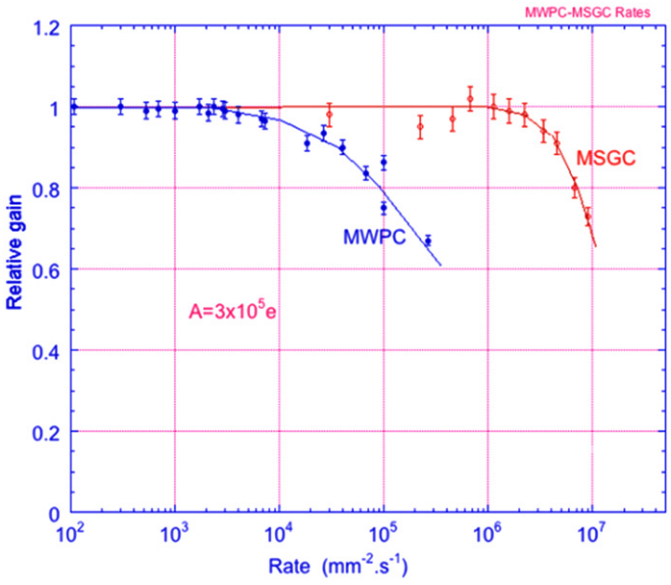

Fig. 34. A comparison of the rate capability of a wire chamber and a micropattern gas detector, A is the amplification factor.

coefficient at high fields, ~ 100 kV/cm in several gas mixtures, thus achieving stable operation with the minimum of ionizing particles at high gains and rates. Large MICROMEGAS detectors have been operational for the COMPASS experiment at CERN and are proposed for the ATLAS Muon upgrade [41]. In Fig. 38 is shown one of the largest size micromegas built.

The electric field distribution is shown in Fig. 37. Drift region has an almost uniform electric field which begins to increase as the field lines approach each other close to the mesh. The region below the mesh is the high field region where amplification occurs as a result of avalanche generation exploiting the exponential rise and subsequent saturation of Townsend coefficient [42]. In Fig. 38 a large area module made with resistive Micromegas by the MAMMA [41] collaboration is shown with details of the assembly and test results in the H6 test beam at CERN.

Another new concept of exploiting gas amplification with a micropattern detector is the gas electron multiplier GEM, manufactured using printed circuit with wet etching techniques. A thin (50 μm) Kapton foil clad on both sides with copper is perforated and the two surface maintained at a potential gradient, thus providing the necessary field for electron amplification, see Fig. 39.

Coupled with a drift electrode above and a read-out electrode below, it acts as a high-performance electron amplifier. The major advantage of this detector is that amplification and detection are decoupled and the read-out is at zero potential. Charge transfer to a second amplification device opens up the possibility of using a GEM in tandem with an MSGC, micromegas or a second GEM. Three GEMs (Fig. 40) may be used in cascade and offer a robust solution for muon tracking and triggering. They are used in the LHCb detector for muon trigger. Highly ionizing particles produce discharges in all micropattern detectors with a typical gain of several thousand. It is possible to obtain higher gains with gases that permit a lower operating voltage and have higher diffusion, thus lowering the charge density and photon feedback probability. At gains of 10^4, spark probabilities as low as 10^{-10} per ionizing particle have been measured. More recently, using single mask production technology [43], large size triple GEM detector prototypes (Fig. 41) have been built and tested by the GEMs for CMS collaboration [44], reporting some performance results (Fig. 42).

High gain up to 10^4 were reached with the large size prototype and space resolution measured very close to the estimated one (strip size/$\sqrt{(12)}$. The prototypes were tested at a 150 GeV muon beam in H2 at CERN with full efficiency in a magnetic field up to 1.6 T. Time resolution of ≈ 5 ns has been measured as shown in Fig. 43.

5.4. *Large volume tracking devices: Time Projection Chamber (TPC)*

The Time Projection Chamber consists of a gas filled sensitive volume, usually with a central high voltage electrode (cathode) that divides the cylindrical volume into two identical halves. Each side has a complete detector with a readout system. The cathode is at a high potential that results in a field strength of 100–500 V/cm while the anodes (readout) are at ground. In 4π-detectors at high energy physics experiments, the drift volume is usually cylindrical and the beam pipe goes through the symmetry axis of the TPC with the interaction point being at the center, although radial TPCs have also been built and have been operational. This combination of a TPC with a gaseous tracking detector on the readout plane has been exploited very successfully in previous experiments at LEP. The principle of the TPC is shown schematically in Fig. 44.

TPC readout With Multiwire Proportional Chambers: the state-of-the-art device is the ALICE TPC in the ALICE 'central barrel', for tracking of charged particles and particle identification.

The ALICE TPC [45] was designed to cope with the highest conceivable charged particle multiplicities predicted for central Pb–Pb collisions at LHC energy, i.e. psuedorapidity densities approaching 8000 per pseudorapidity bin at center-of-mass energy of 5.5 TeV. Its acceptance covers 2π in azimuthal angle and a psuedorapidity interval $|\eta| < 0.9$. Including secondaries, the above charged particle psuedorapidity density could amount to 20,000 tracks in one interaction in the TPC acceptance.

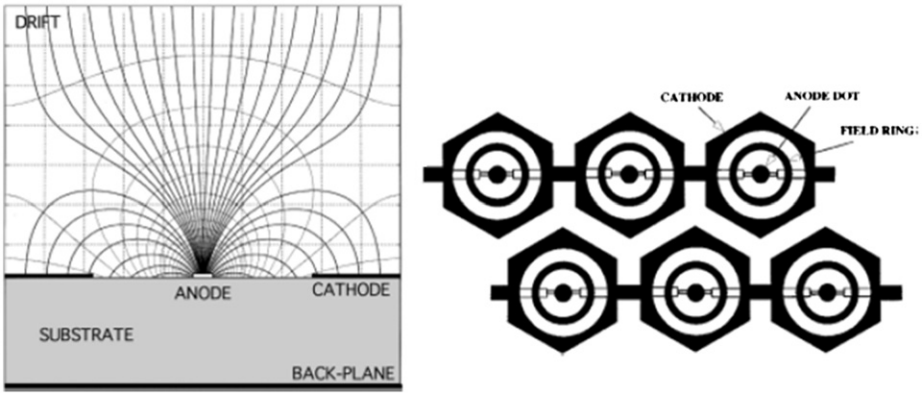

Fig. 35. Schematics of a microstrip gas chamber and a microdot detector.

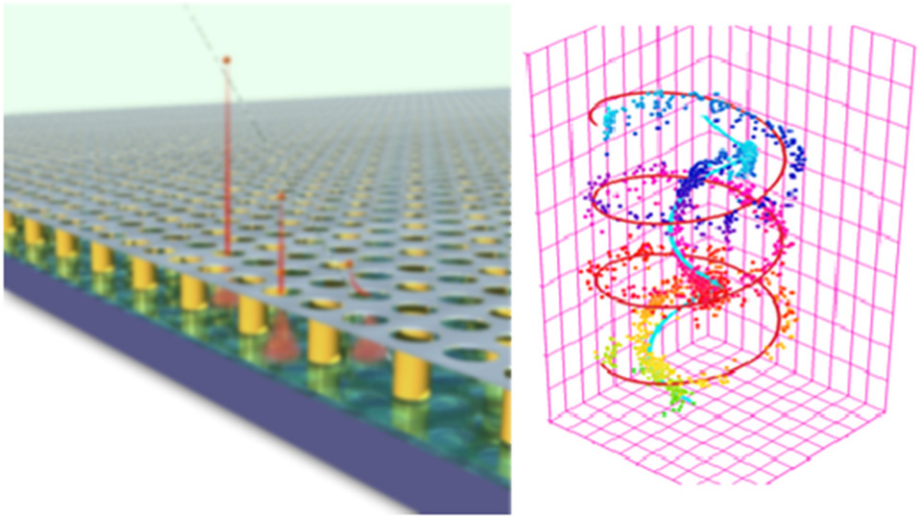

Fig. 36. The GOSSIP detector; two beta's from Sr^{90} measured in a 0.2 T magnetic field.

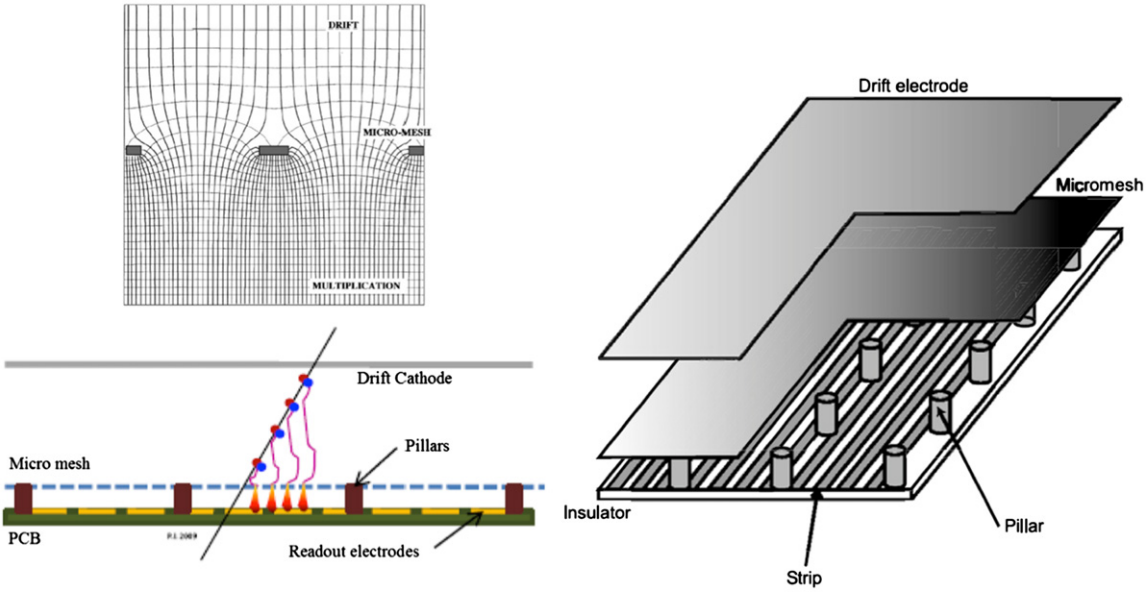

Fig. 37. (Top left) Electrical field, (bottom left) schematics, (right) electrode readout.

This central tracker (see Figs. 45 and 46) is a 88 m^3 cylinder filled with gas and divided in two drift regions by the central electrode located at its axial center. The field cage ensures the uniform electric field along the z-axis. Charged particles traversing the TPC volume ionize the gas along their path, liberating electrons that drift toward the end plates of the

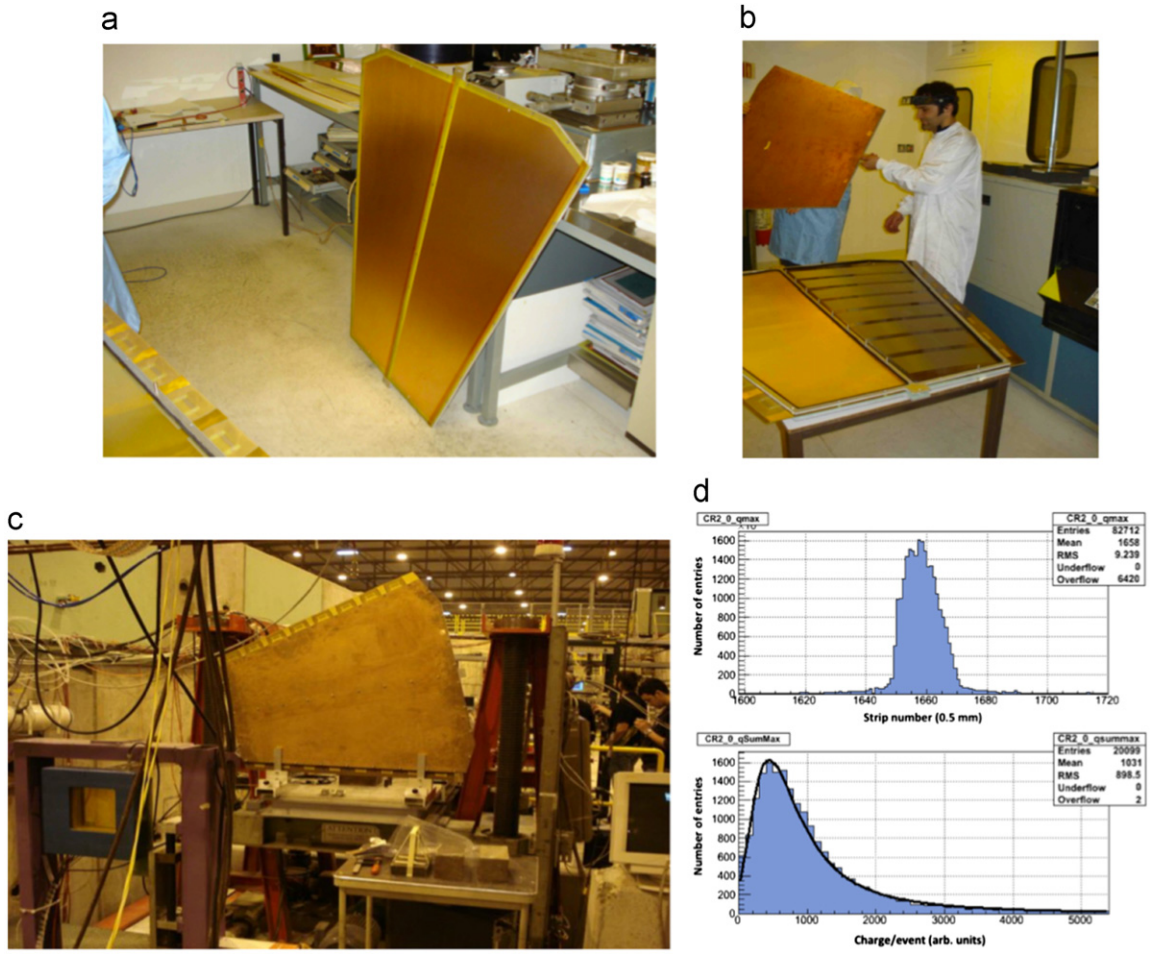

Fig. 38. (a) A large area module made with resistive Micromegas by the MAMMA collaboration. (b) Assembly of large resistive micromegas only the right half is instrumented. (c) Large resistive micromegas chamber in H6 test beam at CERN (d) hit distribution (on top) showing the beam profile and the charge distribution (bottom), adding all charges, showing essentially a Landau shape.

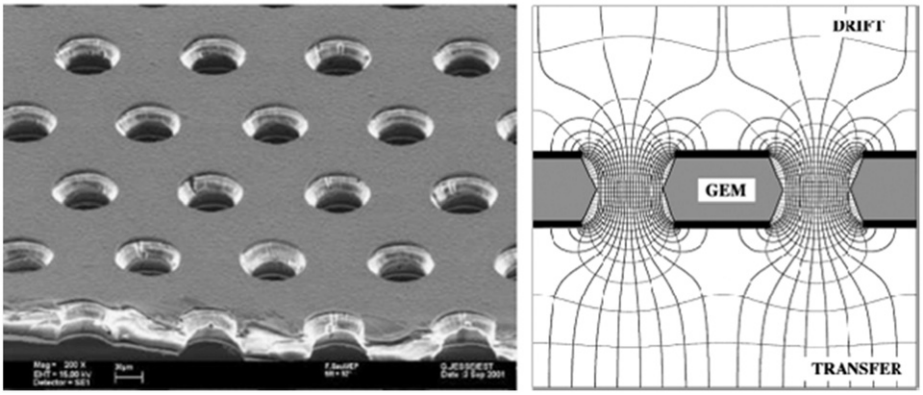

Fig. 39. A GEMs foil and fields across the GEM with the drift region above and transfer below.

cylinder. The necessary signal amplification is provided through an avalanche effect in the vicinity of the anode wires strung in the MWPC readout.

At high rates, space charge distortion in the drift volume is a major factor limiting the performance of a TPC. While the space charge buildup from the primary ionization is inevitable, the positive ions coming from the amplification region should be minimized. Hence, the readout of TPCs with MPGDs is very attractive, the intrinsic ion feedback (sometimes called backflow) suppression of the MPGD allows to reduce the ions escaping into the drift volume to a minimum. Furthermore, effects limiting the spatial resolution in MWPC devices do not exist or are at a minimum in MPGDs, for example loss of signal due to the ExB-effecting the vicinity of the high fields of wires. Several studies have been reported with reduced ion-feedback in GEM-based detectors [46].

Therefore, a number of smaller and larger experiments are studying the use of MPGD based TPCs, e.g. currently two of the three detector concepts for the International Linear Collider are studying such a device as central tracker and a large number of studies have been performed as shown in Figs. 47–49.

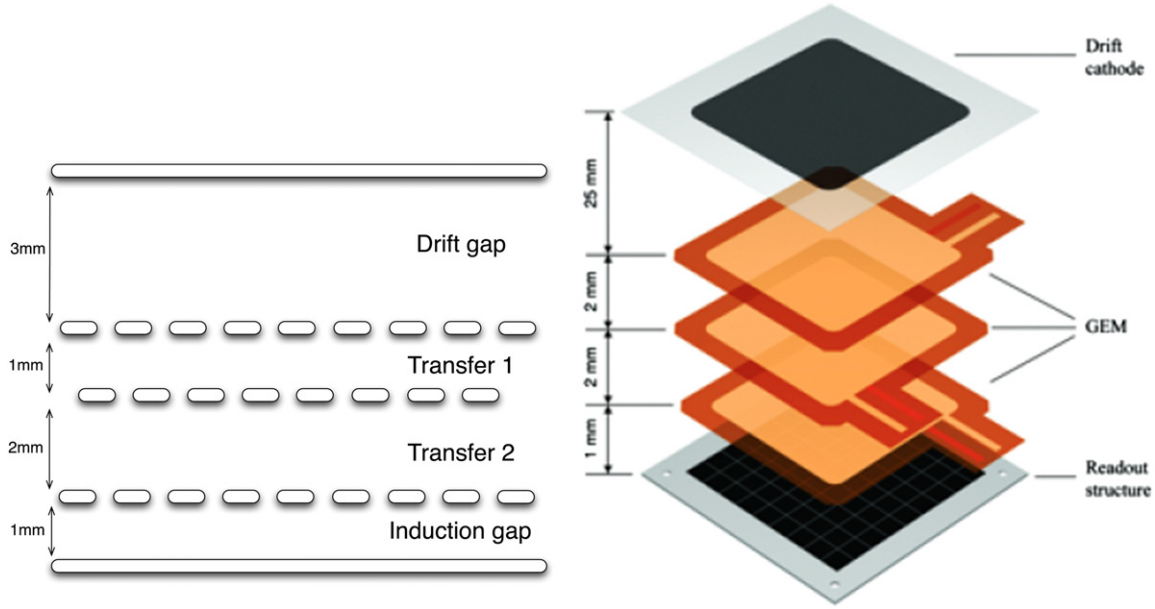

Fig. 40. GEMs come in multiple configurations, double or triple GEM detectors depending on the number of amplifying stages used.

Fig. 41. GEM foil production and test setup at the beam area.

Spatial resolution is determined by the pad/strip size and pitch; in particular the angular pad effects limit the spatial resolution of tracks passing at an inclination with respect to the long axis of a rectangular pad. Hence a decrease in pad size is beneficial for large systems.

6. Aging and sustained long-term operation

Gaseous detectors have been in use since the last few decades and experience has shown that the phenomenon of aging sometimes inhibits long-term operation. This can be due to the deposits on anode wires or on the cathodes of the detector mostly due to the polymerization of the hydrocarbons in the operational gas mixtures used. Following a concerted effort in the studies of gas mixtures, strict recommendations have been made on their composition and purity [48]. Similar recommendations have been made for materials that may be used during the chamber assembly so that there is no out-gassing that could adversely affect chamber operation [49,50]. Quality control and quality assurance have nowadays become an integral part of construction. At LHC the doses that muon chambers will absorb are a few orders of magnitude higher than previous experiments. A comparison of particle rates in different experiments is shown in Fig. 50. Therefore, a significant increase in radiation tolerance is required for the new generation of detectors operating at LHC, its upgrades and future colliders.

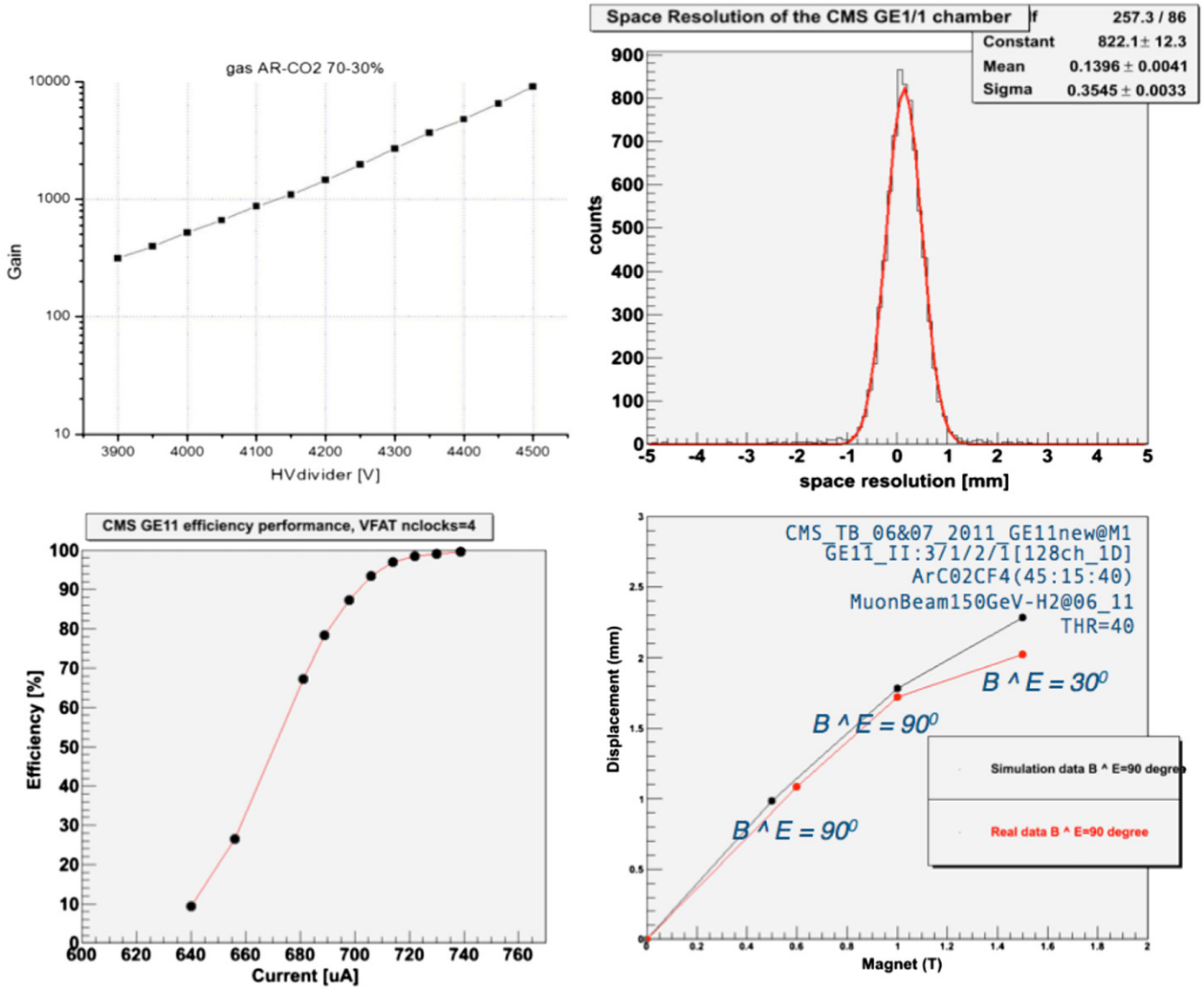

Fig. 42. GEM performance in 2010-2011 CMS-RD51 test beams.

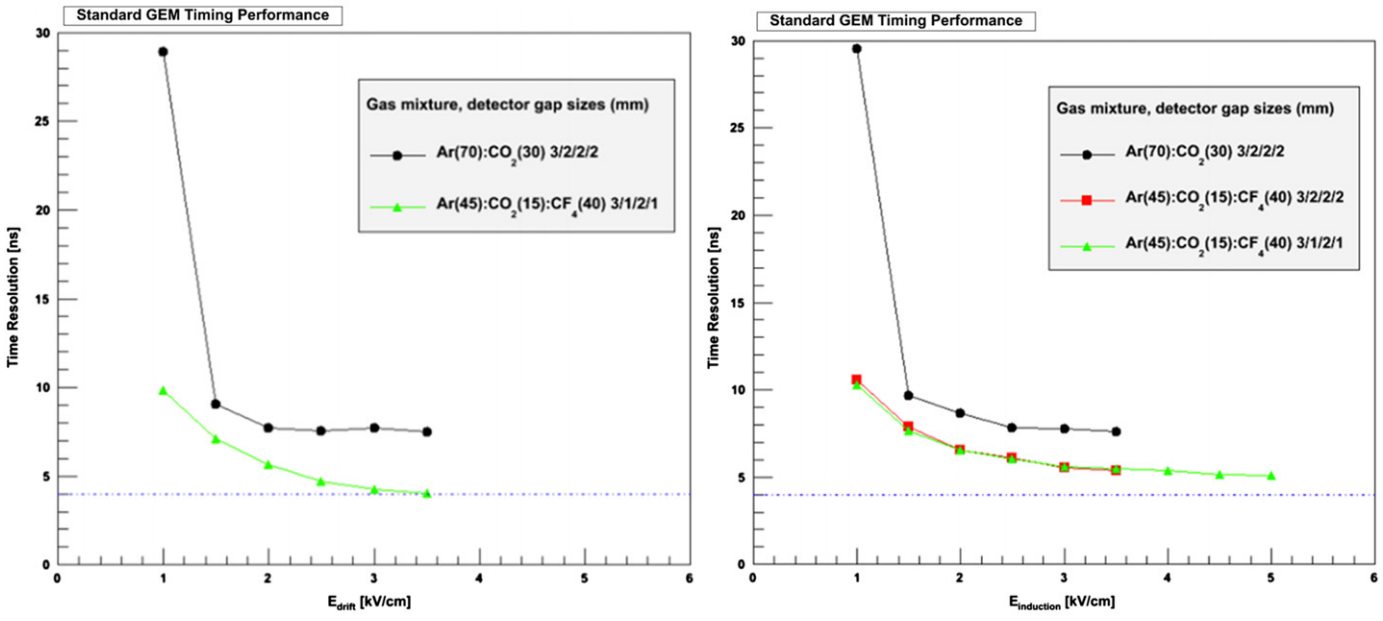

Fig. 43. GEM timing resolution as function of the induction (left) and drift (right) field for the standard triple-GEM with different gas mixtures and gap size configurations.

6.1. Classical wire chamber aging

Due to the formation of deposits on anode wires, the chamber performance is degraded and issues such as gain loss and hence efficiency loss creep up during the lifetime of a wire chamber. Sparks and discharges may be induced due to the charging up of the polymers or 'whiskers' that start growing on the electrodes, a few examples are shown in Fig. 51 [50].

The coating on the wires may be damaged by free and reactive radicals resulting from cracking of the gas mixture. The Malter effect is another particularly catastrophic example of aging which can inhibit long-term operation of a gas detector. This is onset and enhanced by insulating coatings on the cathodes due to polymerizing radicals. These coatings may enhance the fields close to the cathodes to far more than nominal resulting in electron emission, which may develop, over time, into a sustained discharge and finally lead to breakdown. Hence material and gas choice is of vital importance; in addition the rate of gas flow (also known as volume exchange) also determines the rate at which polymers can be flushed out and injection of fresh gas mixture may delay aging. All this also constitutes an operational cost when dealing with very large systems. Some excellent reviews on wire chamber aging may be found in the proceedings of the workshops held in 2001 and 2006. Long-term tests are usually performed in order to validate a chamber production chain for mass construction. Aging has been found to depend on the radiation type and size of the irradiated area, rate of irradiation, operational gas gain and charge density, gas composition and the presence of known (and unknown) trace pollutants, gas volume exchange rate and the patter in which gas flow takes place. Hence validation tests tend to be long and although accelerated representative tests are necessary, nevertheless the results of these tests are indicative. As an example extensive tests on RPCs were performed at the Gamma Irradiation Facility at CERN to validate the detector production for LHC. Typical 5–7 years of LHC equivalent operation were simulated with an important investigation and conclusion of the effect of the operating conditions on the resistivity of Bakelite which decreases with high temperature and increases with low humidity; hence RPCs at ATLAS and CMS are operated a relative humidity of 50% and temperatures lower than (24 °C). Some results [51] of dependence of chamber current, over long period of time, from temperature, humidity and pressure are shown in Fig. 52.

RPC aging effects [52] are not classical aging effects rather random surface deterioration caused by trace pollutants. Hence surface quality of RPC electrodes is crucial for long-term operation. Some results on investigations of surface quality improvements are shown in Fig. 53.

As an example of micropattern detector aging for triple GEM long-term operation case has been demonstrated by the group of LHCb. The accumulated charge is shown in Fig. 54. Detectors

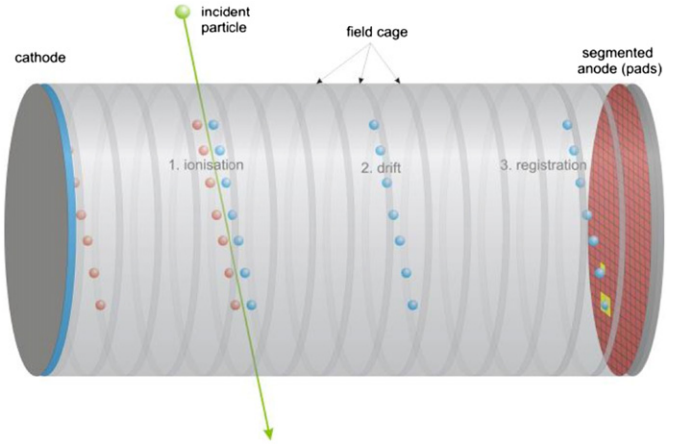

Fig. 44. Schematic of a Time Projection Chamber.

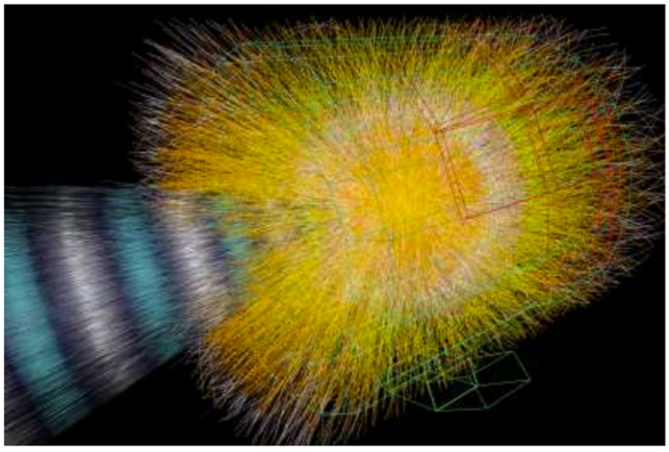

Fig. 46. ALICE TPC during data-taking.

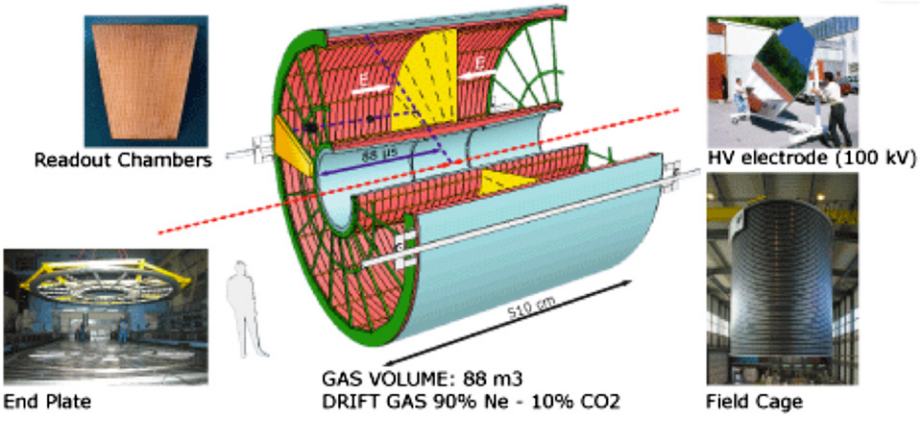

Fig. 45. Details of the ALICE Time Projection Chamber.

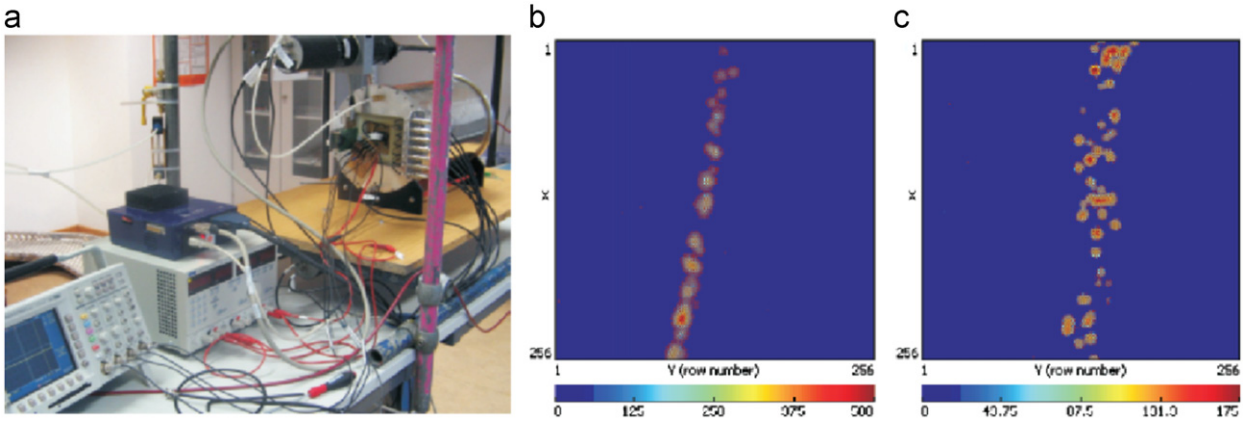

Fig. 47. Prototype detector of a TPC with triple GEM and Pixel-ASIC readout: (a) photograph of a cosmic ray test setup, (b) signal of track passing through the detector close to the readout, (c) close to the cathode.).

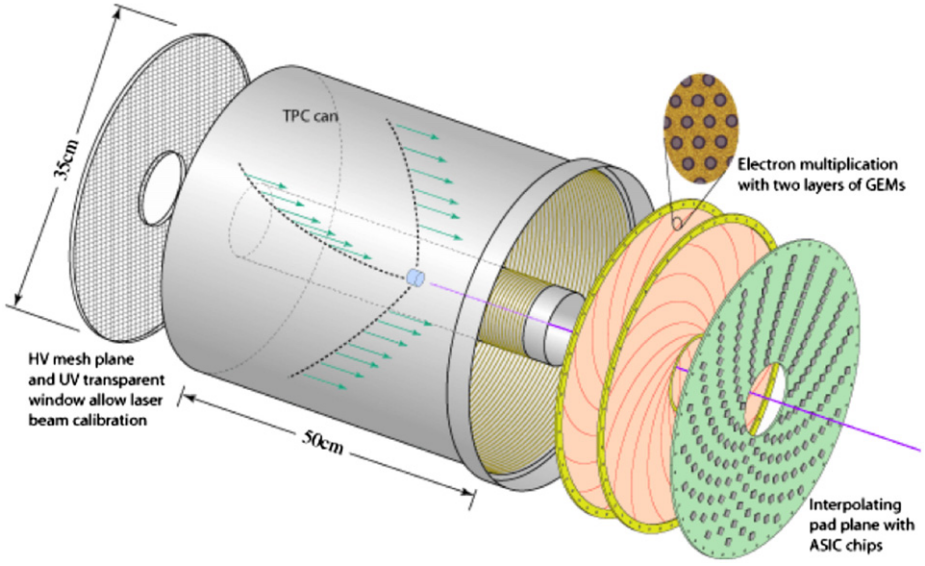

Fig. 48. The schematic view of the LEGS [47] is shown below.

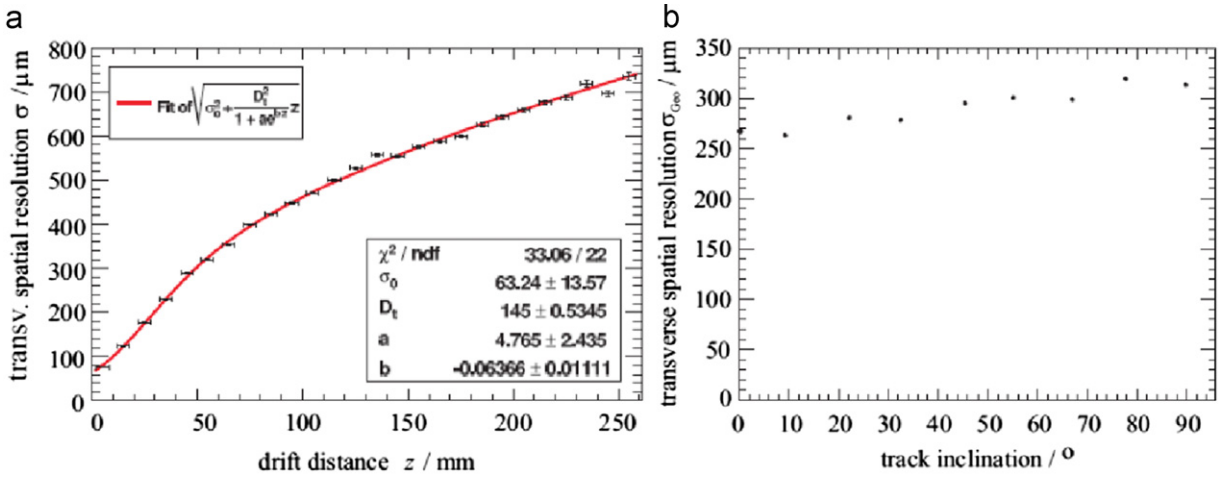

Fig. 49. TPC with triple GEM and Pixel-ASIC readout. Transverse spatial resolution in dependence on: (a) drift distance, (b) track inclination in the readout plane.

hydrocarbons, although a very popular quenching component of operational gas mixtures, are prone toward polymerization and hence alternatives need to be found. Argon, carbon dioxide and CF_4 based mixtures, typically used for RPCs, are quite common and have been proven to be radiation tolerant. Freon and SF_6 based mixtures crack in the presence of radiation and may form

HF-ions and in combination with even trace amounts of oxygen and water can be detrimental to chamber operation [53].

The major goals and concerns for muon detectors at the ILC are similar to those for LHC upgrades namely, high efficiencies of muon detection and low sensitivity to backgrounds. A good time resolution resulting in unambiguous bunch separation and backgrounds rejection combined with precise coordinate resolution would result in an optimal matching of a track from the central tracker with hits from the muon system hits. The momentum resolution of high energy muons ($\sim 0.1-1$ TeV) is limited by multiple scattering. Drift tubes, Resistive Plate Chambers and micropattern detectors and other variants are being considered. Detailed aging studies will be necessary to validate the performance of these detectors in the hostile radiations environments at a rate of 1–15 kHz/cm^2 and over a Mrad of dose.

7. Gas mixture optimization

For tracking at the high luminosity hadron collider like LHC, an operational gas mixture has the following pre-requisites: an operational gas mixture should ideally be characterized by high drift velocity associated with a large primary ionization yield. The drift velocity would ideally be saturated or have a small variation with modifications in electric and magnetic fields. The mixture needs to be well quenched with no secondary effects like photon feedback and field emission giving a stable gas gain well separated from the noise of the electronics. Fast ion mobility for quick clearance of positive ions to inhibit space charge effects also helps in having small EXB effects whereby the trajectory of the electrons follows the Lorentz angle in high electric fields. A good

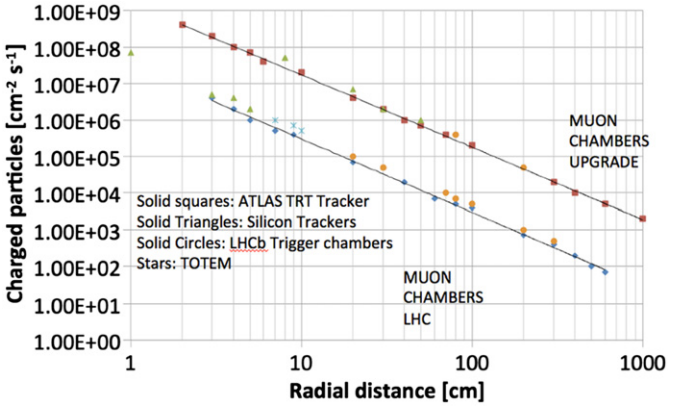

Fig. 50. Measured and expected particle rates as a function of radial distance to the beam axis for various experimental conditions. Include ILC, HL-LHC.

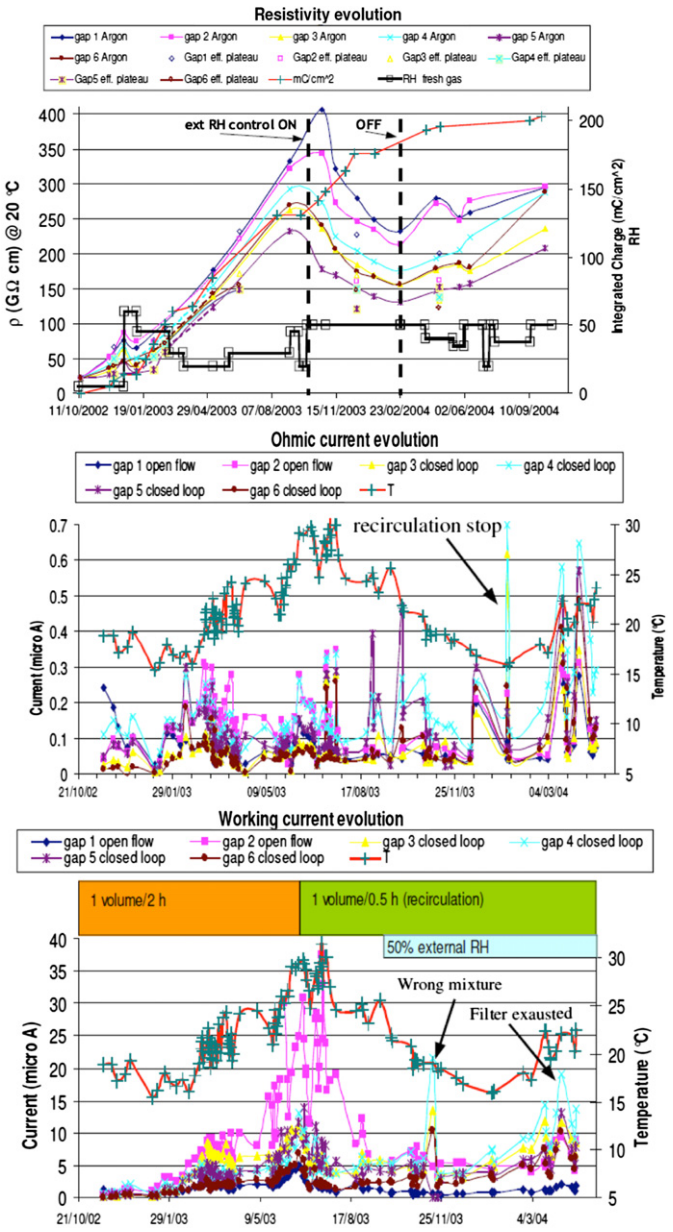

Fig. 52. Long-term operation of the RPCs at GIF: resistivity evolution over 2 years; Ohmic current increases can be related to internal surface damage (existing defects, presence of pollutants); working current increases can be related to temperature (reversible) and to any malfunctioning of the gas system (insufficient total flow, recirculation filters exhaustion, wrong mixture). Damage recovery procedures such as flushing with Argon and lower-voltage operation with isobutane enriched mixtures were successfully concluded.

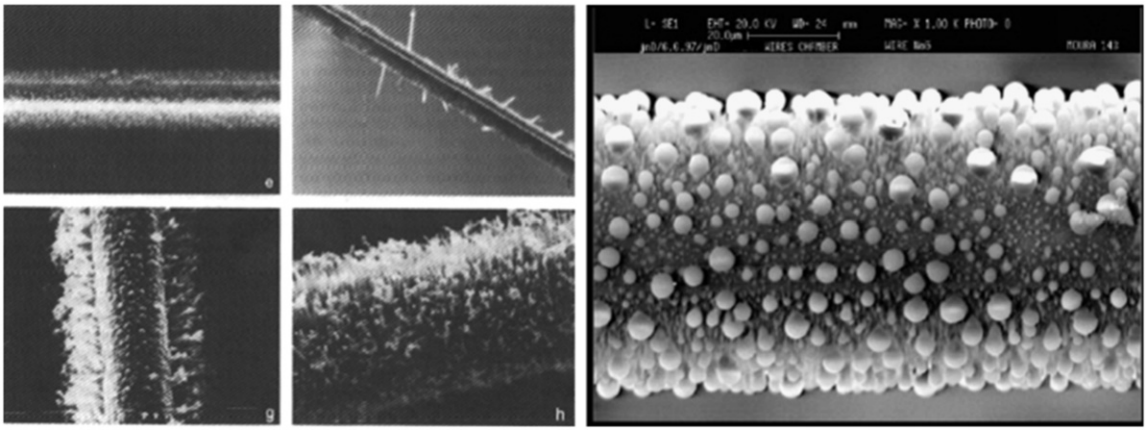

Fig. 51. Examples of wire deposits and whisker formation.

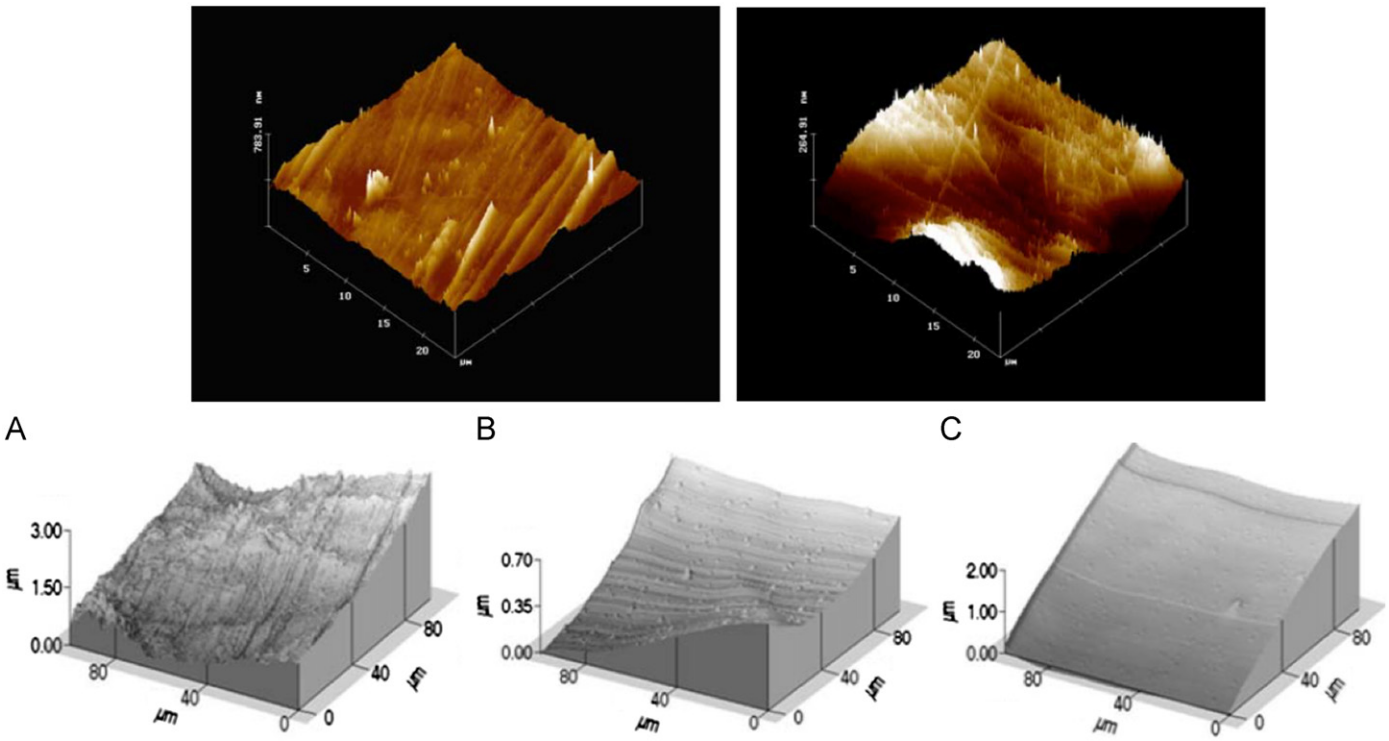

Fig. 53. Surface quality of (top left) Beijing phenol/melamine plastic laminate and (top right) Italian LHC like phenol/melamine plastic laminate. Comparison of the three photos (bottom) demonstrate the successive surface improvement due to the deposition of a uniform linseed oil layer; the scale is in μm.

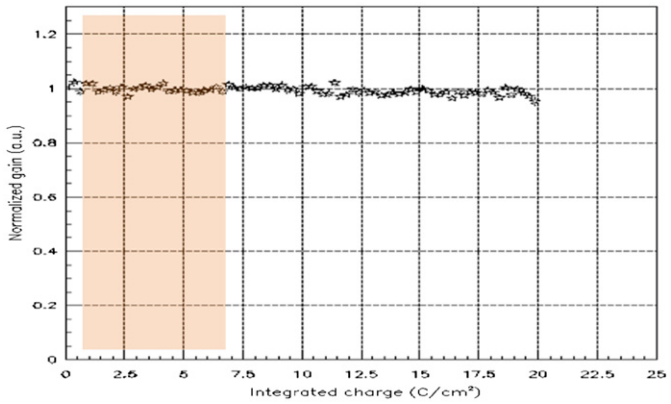

Fig. 54. Aging studies for triple GEMs. The shaded region shows the integrated charge expected for the upgrades at LHC [54].

review of gas transport parameters may be found in Ref. [55]. Clearly financial constraints also need to be addressed in large gas systems, and a nonflammable, eco-friendly gas mixture is often a pre-requisite for safety.

7.1. Statistics of electron–ion pairs production in gas

When an ionizing particle passes through a gas free electrons, ions are produced in amounts that depend on the atomic number, density and ionization potential of the gas, and on the energy and charge of the incident particle. The number of primary electron pairs per cm is usually indicated with Np. The created electrons may have sufficient energy to ionize further and create secondary electron–ion pairs. The overall outcome of the two processes is called total ionization, the total number of electron–ion pairs per cm is denoted by Nt. Np and Nt depend on incident particle charge and velocity, and are characteristic of a given gas or gas mixture. They affect the localization accuracy and in particular for thin gas gap chambers the accuracy is largely affected by the average distance between primary ionization clusters. These numbers have been measured and computed for a variety of gases. Table 6 lists some values for Np and Nt, along with other general gas properties. All numbers are for normal temperature and pressure (NTP).

7.2. Electron transport properties

Rigorous treatment of the theory of electron transport has been extensively summarized in the various references quoted; here it is very simply reminded without mathematical detail. When the electrons move in an electric field they may still attain a steady distribution if the energy gained per mean free path is small compared with the electron energy. The momentum transfer per collision is not a constant, especially in excitation and ionization collisions between electrons and atoms, causing a larger energy loss. Electrons with energies near the Ramsauer minimum in argon (see cross-section of Argon) for example (0.23 eV) have long mean free paths and as a consequence, can gain more energy before experiencing a collision with the surrounding gas. This is taken into account in computing the energy distribution function and has consequences on the gas parameters. The drift velocity is also dependent on pressure, temperature and can be modified by the presence of pollutants like water or oxygen (as will be demonstrated in Section 5); electronegative pollutants deplete the gas of electrons.

Differently from noble gases, poly-atomic molecular and organic gases have many other modes of dissipating energy, namely molecular vibrations and rotations. The probabilities of these mechanical excitations can be as important as those of

Table 6
Basic properties of some gas mixtures typically used in gaseous detectors.

Gas	Ratio	Density$*10^{-3}$ (g/cm^3)	Radiation Length (m)	Np (cm^{-1})	Nt (cm^{-1})
He		0.178	5299	4.8	8
Ar		1.782	110	24.3	94
Ne		0.9	345	12	43
Xe		5.86	15	44	307
CF_4		3.93	92.4	51	100
DME		2.2	222	60	160
CO_2		1.98	183	35.5	91
CH_4		0.71	646	26.5	53
C_2H_6		1.34	340	41	111
i-C_4H_{10}		2.59	169	84	195
Ar-CH_4	90–10	1.67	120	24.5	90
	80–20	1.57	132	24.7	85.8
	70–30	1.46	147	25	82
Ar-C_2H_6	90–10	1.74	118	26	95.7
	80–20	1.69	127	27.6	97.4
	70–30	1.65	138	29	99.1
Ar-iC_4H_{10}	90–10	1.86	114	30.27	104.1
	80–20	1.94	118	36.24	114.2
	70–30	2	122.8	42.21	124.3
Ar-CO_2	90–10	1.8	114.5	25.42	93.7
	80–20	1.82	119.5	26.54	93.4
	70–30	1.84	124.9	27.66	93.1
He-CH_4	90–10	0.237	3087	7	12.5
	80–20	0.285	2178	9.1	17
	70–30	0.355	1683	11.3	21.5
He-C_2H_6	90–10	0.29	2155	8.42	18.3
	80–20	0.41	1353	12	28.6
	70–30	0.53	986	15.6	38.9
He-iC_4H_{10}	90–10	0.42	1313	12.7	26.7
	80–20	0.66	749	20.6	45.4
	70–30	0.9	524	28.6	64.1
He-CO_2	90–10	0.358	1396	8	16.3
	80–20	0.538	804	10.9	24.6
	70–30	0.719	565	14	32.9
Ne-CH_4	90–10	0.881	361.8	13.45	44
	80–20	0.862	380.4	14.9	45
	70–30	0.843	401	16.35	46
Ne-C_2H_6	90–10	0.0944	344	14.9	49.8
	80–20	0.988	343.9	17.8	56.6
	70–30	1.032	343.4	20.7	63.4
Ne-iC_4H_{10}	90–10	1.06	312	19.2	58.2
	80–20	1.23	285	26.4	73.4
	70–30	1.4	262	33.6	88.6
Ne-CO_2	90–10	1	317	14.35	47.8
	80–20	1.12	293	16.7	52.6
	70–30	1.22	272	19	57.4
Xe-CH_4	90–10	5.34	16.6	42.25	281.6
	80–20	4.83	18.6	40.5	256.2
	70–30	4.31	21.2	38.75	230.8
Xe-C_2H_6	90–10	5.4	16.6	43.7	287.4
	80–20	4.95	18.5	43.4	267.8
	70–30	4.5	21	43.1	248.2
Xe-iC_4H_{10}	90–10	5.53	16.5	48	295.8
	80–20	5.2	18.3	52	284.6
	70–30	4.87	20.6	56	273.4
Xe-CO_2	90–10	5.47	16.5	43.15	285.4
	80–20	5.1	18.4	42.3	263.8
	70–30	4.69	20.7	41.45	242.2

electronic excitations. The actual mechanism of such interactions is complex and the molecule can be in a final state very different from the ground state of the molecule. For instance, for carbon dioxide these collisions are produced at relatively small energies (0.1–1 eV) compared to excitation and ionization collisions, see Fig. 55. The vibrational and rotational excitation cross-sections results in an increase in the mean fractional energy loss and a decrease in the mean electron energy. The mean or 'characteristic electron energy' represents the average 'temperature' of the drifting electrons: a gas may be called warm or cold depending upon the average electron energies being above the mean energy limit, in the electric field range considered.

As the electrons are drifting in the electric field they also disperse, thus giving rise to volume diffusion, transverse and longitudinal to the direction of motion. In cold gases like carbon-dioxide for example, the diffusion is small, while drift velocity is low and unsaturated for values of electric fields usual in gas detectors; this implies a non-linear space time relation. Warm gases like argon, for instance, have a higher diffusion; when mixed with polyatomic/organic gases having vibrational thresholds between 0.1 and 0.5 eV, diffusion is reduced in most cases, while the drift velocity is increased. Clearly, due to the deflection effect exerted by a magnetic field perpendicular to the electric field and the motion of the electron, the electron moves in a

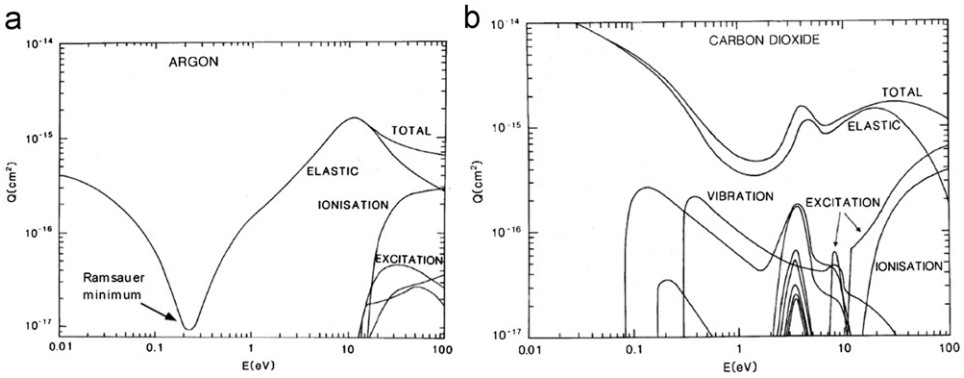

Fig. 55. Electron collision cross-sections in Argon (a) and carbon dioxide (b).

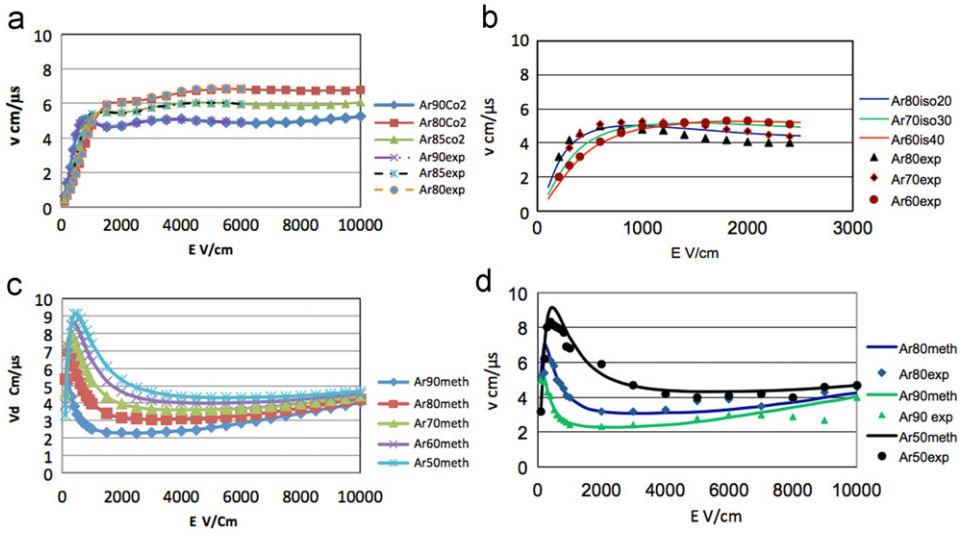

Fig. 56. (a) The drift velocity of Ar/CO_2 mixture for different percentages using Garfield + exp data, (b) the drift velocity of Ar/iC_4H_{10} mixture for different percentages using Garfield + exp data, (c) the drift velocity of Ar/CH_4 mixture for different percentages using Garfield, (d) the drift velocity of Ar/CH_4 mixture for different percentages using Garfield + exp data.

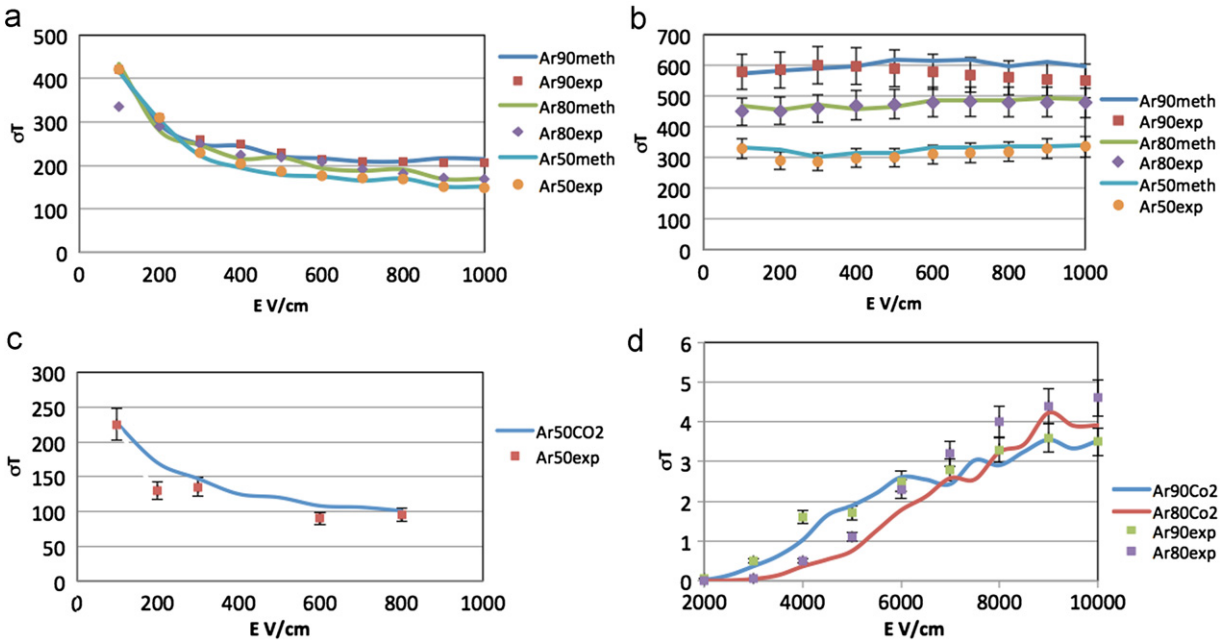

Fig. 57. (a) Longitudinal diffusion of Ar/CH4 mixture for different percentages using Garfield + exp data, (b) transverse diffusion of Ar/CH_4 mixture for different percentages using Garfield + exp data, (c) transverse diffusion of Ar/CO_2 (50–50) mixture using Garfield + exp data, (d) attachment coefficient of Ar/CO_2 mixture using Garfield + exp data.

Table 7
Rates at CMS and ATLAS muon trigger.

Gas	Ion	Mobility ($cm^2/V\,s$)
Ar	Ar^+	1.00
Ar	Methylal$^+$	1.51
iC_4H_{10}	Methylal$^+$	0.55
Methylal	Methylal$^+$	0.26
iC_4H_{10}	$iC_4H_{10}^+$	0.614
Ar	CH_4^+	1.87
CH_4	CH_4^+	2.26
Ar	CO_2^+	1.72
CO_2	CO_2^+	1.09
C_2H_6	$C_2H_6^+$	1.23–1.24
CF_4	$C_2H_6^+$	1.04
C_3H_8	$C_3H_8^+$	0.793
CF_4	CH_4^+	1.06–1.07
DME	DME$^+$	0.56
CF_4	$C_2H_6^+$	1.04
CF_4	$C_3H_8^+$	1.04–1.05
CF_4	iC_4H_{10}	1.00
Ar	CH4$^+$	2.07–1.87
Ar	C2H6$^+$	2.06–2.08
Ar	C3H8$^+$	2.08–2.07
Ar	iC_4H_{10}	2.15–1.56

helical trajectory resulting in a lowered drift velocity and transverse dispersion. Thus the arrival time of electrons in a proportional counter for example changes and the spread in the drift time increases.

The angle which the drifting electron swarm makes with the electric field is defined as the Lorentz angle of the particular gas or gas mixture under consideration. This depends on both the electric field and the magnetic field. It is normally large at small electric fields but falls to smaller values for larger electric fields and is approximately linear with increasing magnetic field. It has been observed that gases with low electron energies have a small Lorentz angle. In the case of a small mis-alignment between the electric and magnetic fields, the resulting drift velocity and transverse diffusion will distort the space time relation at the ends of the drift space in both TPC end-cap multiwire chambers and drift chambers in a magnetic field. Therefore these effects have to be carefully studied and minimized.

Calculations [15] can now be routinely carried out with the MAGBOLTZ computer program for transport parameters developed by Biagi [34]. The program was initially developed as a multiterm Boltzmann expansion allowing the extraction of the absolute cross-sections for electron scattering from the experimental data on drift velocity and transverse diffusion. Data from inelastic scattering cross-sections are also used; some examples of drift velocity and diffusion are shown in Figs. 56 and 57, with some comparisons to experimental measurements.

7.3. Ion transport properties

The ion mobility is defined as the ratio of drift velocity (v_i) of the ions and the reduced electric field (E/p), in the absence of magnetic field, where E and p are the electric field and pressure respectively; it is almost constant up to rather high fields being specific to a particular ion moving in a specific gas. Table 7 shows the ion-mobility at atmospheric pressure of some commonly encountered gas molecular ions.

7.4. Dependence of transport parameters on pollutants

The presence of pollutants in the operating gas mixture affects the gas detector operation as well. There are two effects: one is the modification of transport parameters and the second is electron loss by capture due to electro-negative pollutants (Fig. 58).

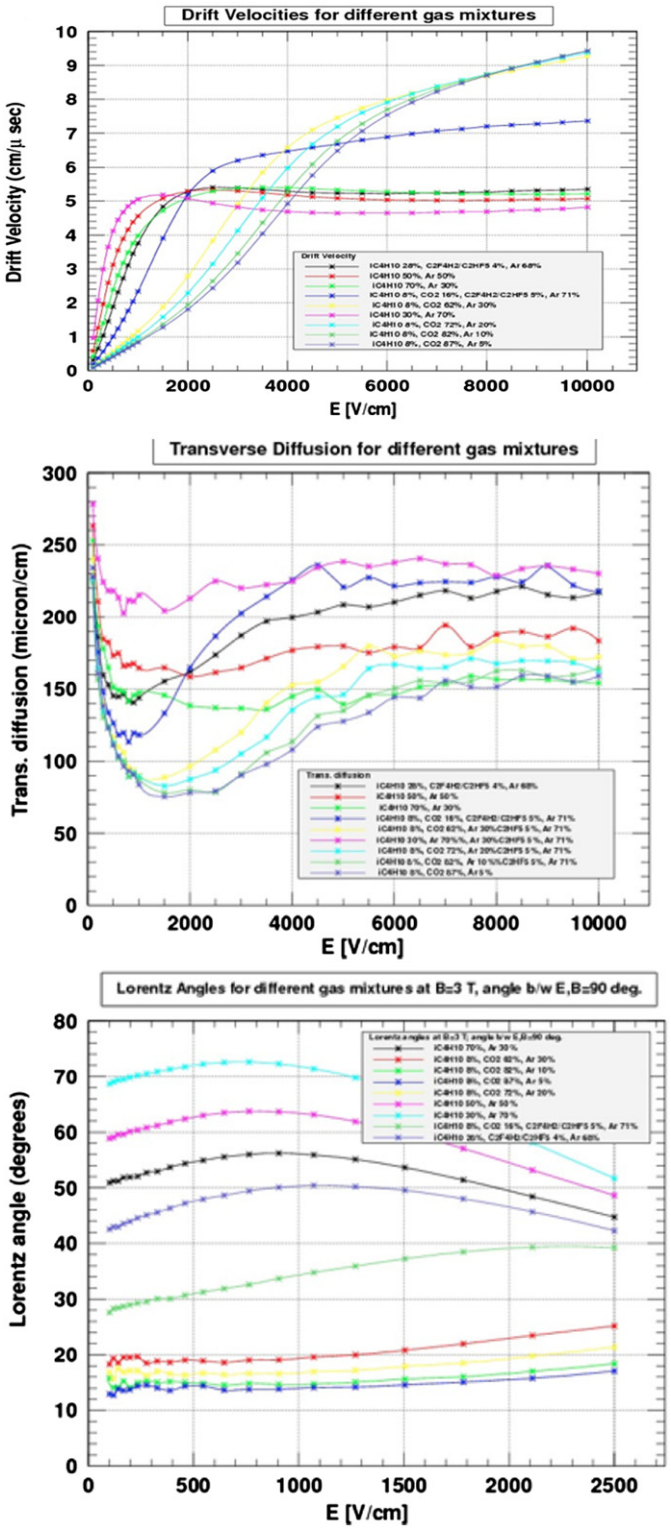

Fig. 58. Transport properties of some RPC gas mixtures.

In the case of addition of water, the static electric dipole moment of the water molecule increases the inelastic scattering cross-section for low energy electrons, thus reducing dramatically the drift velocity. Fig. 59 shows measurements of drift velocity [44] exemplifying the effect of impurities in the gas mixture. The measured drift velocity in Ar/CO_2 85/15 with a relative content of $0{,}15O_2$, $0{,}6N_2$ and $0{,}5O_2$, $2N_2$ compared to clean Ar/CO_2 (constant pressure). A significant difference can be seen between the clean

gas and the other two gas mixtures. An electron capture (attachment) phenomenon has also a non-negligible electron detachment probability, and the transport parameters may also be sensitive to this electron slowing down mechanism.

The electron attachment coefficient C_{en}, M, may be defined as

$$A = PM \times Pen \times C_{en},M \tag{9}$$

where A is the attachment rate, PM and Pen are the partial pressures of the gas, and that of the electronegative impurity. The units of C_{en}, M are usually (bar^{-2} μs^{-1}), thus if the total drift length in a large detector is measured say in 50 μs, an attachment coefficient of 500 represents a loss of 10% in gain per ppm of electronegative pollutant. The gain loss per ppm of oxygen as a function of attachment coefficient of several gas mixtures has been estimated from several measurements [45,46]. The mean capture length is λ estimated and is shown in Table 8, p being the fraction of oxygen in the mixture. For $p=0.01$ we have for Xenon a λ_p of 0.8 cm, while for warm gases this number is quite small. For cold gases however, it is difficult to drift to large distances without electron capture, as seen from the attachment coefficients; this may impose serious requirements on the purity of the gas.

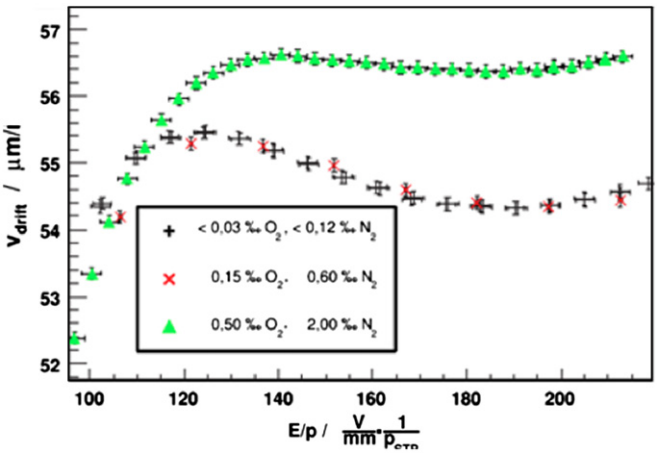

Fig. 59. Dependance of impurity on drift velocity.

Table 8
Mean capture length λ_p for some gas mixtures.

Gas mixture	Electric field (V/cm^2)	λ_p (cm)
Ar–CH_4 (90–10)	150	5.1×10^{-2}
Ar–CH_4 (90–10)	250	3.4×10^{-2}
Ar–CH_4 (80–20)	100	1.6×10^{-2}
Ar–CH_4 (80–20)	200	2.9×10^{-2}
Ar–CH_4 (80–20)		9.3×10^{-2}
Xe–CH_4 (90–10)	≈500	7.8×10^{-2}

8. Applications

Apart from muon detectors in large experiment, gaseous chambers have been used for a variety of applications in and outside particle physics, for example in X-ray imaging, medical and plasma diagnostics, space applications, crystallography and small angle scattering, and so on. In this section for completeness, we briefly give only some examples where gaseous detectors are being exploited.

8.1. Digital hadron calorimetry

The novel concept of particle flow that is being investigated for the readout of calorimetry (hadron and electromagnetic) for the ILC is to use number of hits instead of deposited energy in the detectors interspersed within large absorbers. This would mean measuring how many and which 'pads' would give a signal over threshold. This would imply a simpler electronics and also simpler requirements on uniformity of the active medium thus reducing the costs of electronics. On the other hand one would need a much higher granularity 1×1 cm^2 requiring then about 70–80 millions of channels. According to simulation studies, it provides a better separation between close showers, and better energy resolution with smaller tails.

Better identification of charged particles with Glass RPC and Micromegas detector is being developed by the CALICE [56] collaboration for digital hadron calorimetry at the ILC. Some examples are shown in figures below (Fig. 60).

The Triple GEM detector [58] has also been proposed for the digital hadron calorimetry, as shown in Fig. 61.

8.2. Thermal neutron imaging

Another kind of micropattern detector: capillary plates (CPs) have been successfully fabricated and tested using collimated thermal neutron beam. The results indicate their sensitivity to thermal neutrons, the intrinsic high spatial resolution of MPGDs

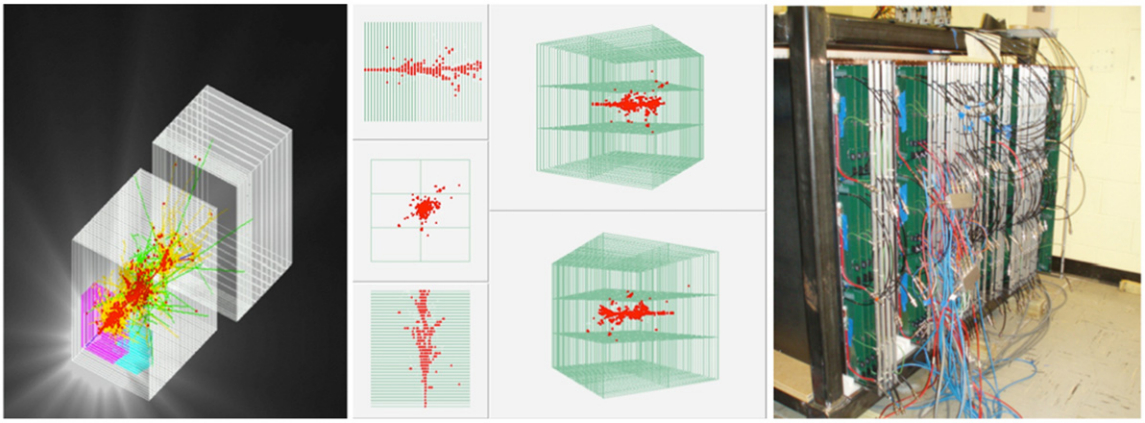

Fig. 60. Simulations (CIEMAT) top, side, front and three-dimensional views of a 32 GeV pi+ event, recorded with DHCAL [57]. In the case of DHCAL, layers of steel alternate with Resistive Plate Chambers, or RPCs, as active elements. Particles traverse the RPCs and ionize the gas inside them, creating a small avalanche, which can be detected with the sensory pads. In a novel version, the Micromegas detector has also been tested for DHCAL.

and high rate capability make them the detector of choice for neutron imaging with high spatial resolution and large dynamic range.

8.3. Single photon detection

Thick GEMs [59] (a thick version of GEM foils) are robust, mechanically stiff and can take advantage of a production technology widely used for printed circuit boards: they are well suited to instrument large surfaces. The space resolution that can be obtained is in the sub millimeter range and the material budget is not particularly increased. These characteristics are fully compatible with the usage of THGEMs for the sensitive elements of digital hadron calorimetry and the design of THGEM based single photon detectors for Cherenkov imaging counters. In the latter application, THGEMs have CsI photocathodes deposited on their surface; the advantage of an architecture based on multiple layers of multipliers (cascaded multipliers), with respect to the presently used MWPCs, is the possibility to limit the ion feedback which can eventually damage the photocathode. In order to reduce or to eliminate discharges, resistive THGEM like (Resistive thick GEM) structures have been studied, namely thick GEMs where the metal conductive electrodes are coated by resistive materials. These structures have been developed to detect single photons in visible sensitive gaseous photomultipliers or for Cherenkov imaging applications.

8.4. Soft X-ray plasma diagnostics using GEM detectors

The GEM detector can also be used to detect X-ray photons. It has been used for imaging the plasma which is essential in the TOKOMAK fusion experiment. The magnetic fusion plasma from

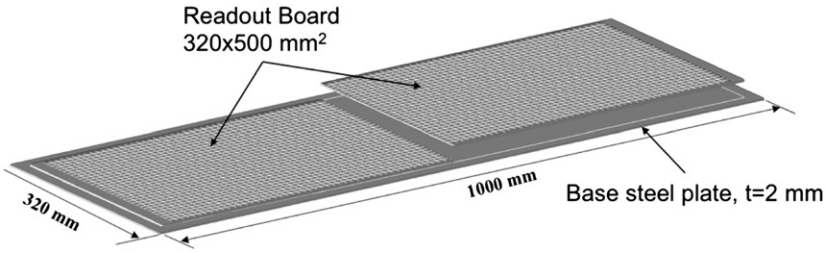

Fig. 61. Triple GEM DHCAL.

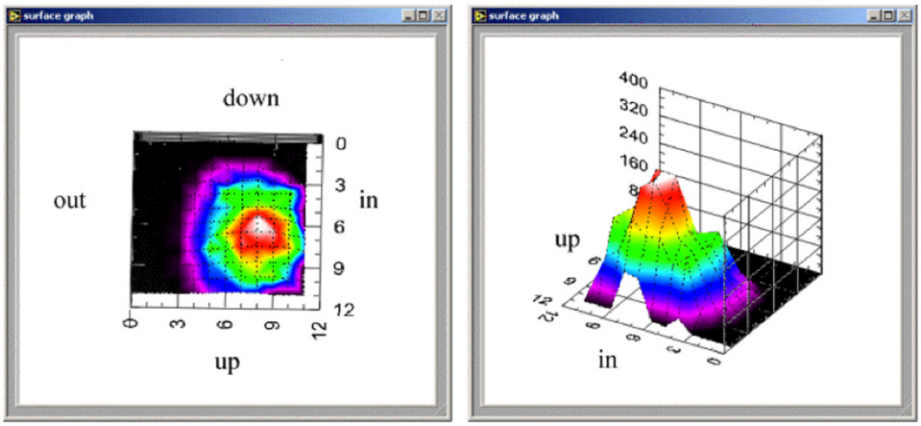

Fig. 62. Example of MPGDs (capillary tube) detector response to X-ray and neutrons.

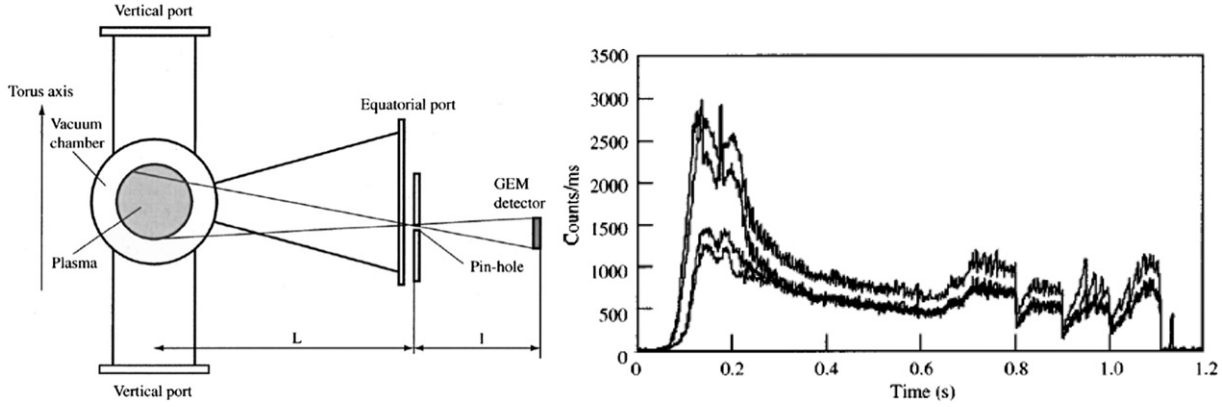

Fig. 63. Example of MPGDs (capillary tube) detector response to X-ray and neutrons.

the TOKOMAK experiment gives X-ray emissions which have been detected using GEMs and has been imaged with a sampling frequency of 20 kHz. The detector performance was found to be operating satisfactorily under the conditions of high rate and large gain as shown in Fig. 62 [60] (Fig. 63).

8.5. RPCs in PET imaging

Resistive Plate Chambers affording excellent space and time resolutions have been studied for their application in the construction of high end imaging [61] systems for Positron emission tomography for the detection of 511 keV photons. An example is shown in Fig. 64.

8.6. Muon detectors used for cosmic ray tomography

Muon detectors have been used in a system designed to analyze the muons produced by the decay of naturally incoming cosmic rays. These muons undergo Coulomb scattering when they pass through an object of a specific material. This scattering is material dependent and hence the detection process helps analyze the same non-destructively.

In a similar application nuclear contraband that is well shielded to absorb emanating radiation can also be detected for homeland security applications using atmospheric muon tomography (MT) based on the measurement of multiple scattering of atmospheric cosmic ray muons traversing cargo or vehicles that contain high-Z material. Due to the excellent spatial resolution of GEMs it is sufficient to use a gap of only a few centimeter between tracking stations. Together with the compact size of the GEM detectors this allows the GEM MT station to be an order of magnitude more compact than MT stations using traditional wire chamber technologies [62] (Fig. 65).

8.7. X-ray polarimetry

Photometry, imaging, spectroscopy, and polarimetry are exploited routinely in X-ray astronomy. A new instrument using X-ray polarimetry derives the polarization information from the track of a photoelectron imaged by a finely subdivided micropattern gaseous pixel detector, as shown in Fig. 66 [63].

8.8. Medical imaging and diagnostics

An online proton beam monitor for cancer therapy based on ionization chambers with micro pattern readout has been developed. In this application a real-time measure of beam parameters

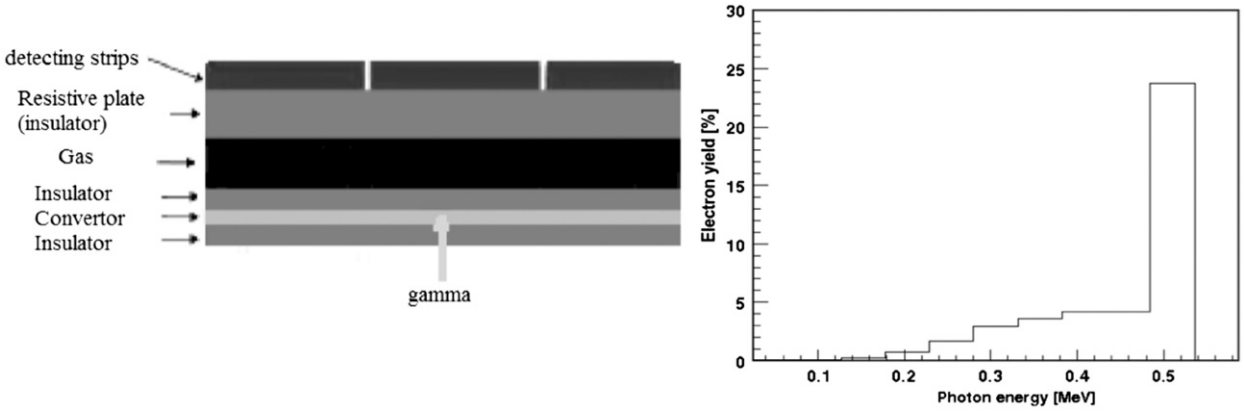

Fig. 64. Schematic detection of gamma rays using RPC for positron emission tomography applications. Electrons collected as a function of the photon energy of the gamma generated by the electron–positron annihilation.

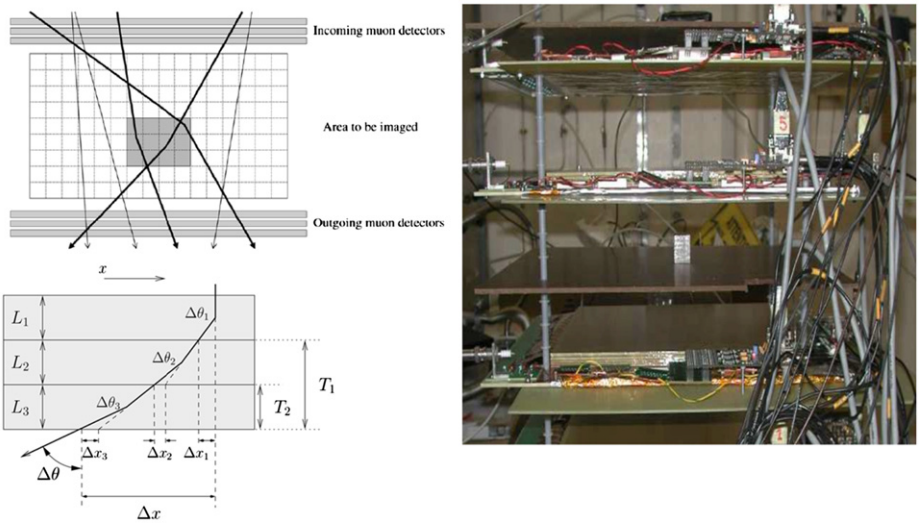

Fig. 65. Example of scattering through multiple layers and the influence of the material properties. Muon tomography system with muon detectors placed at the incoming and outgoing ends and the scattering processes can be identified a prototype.

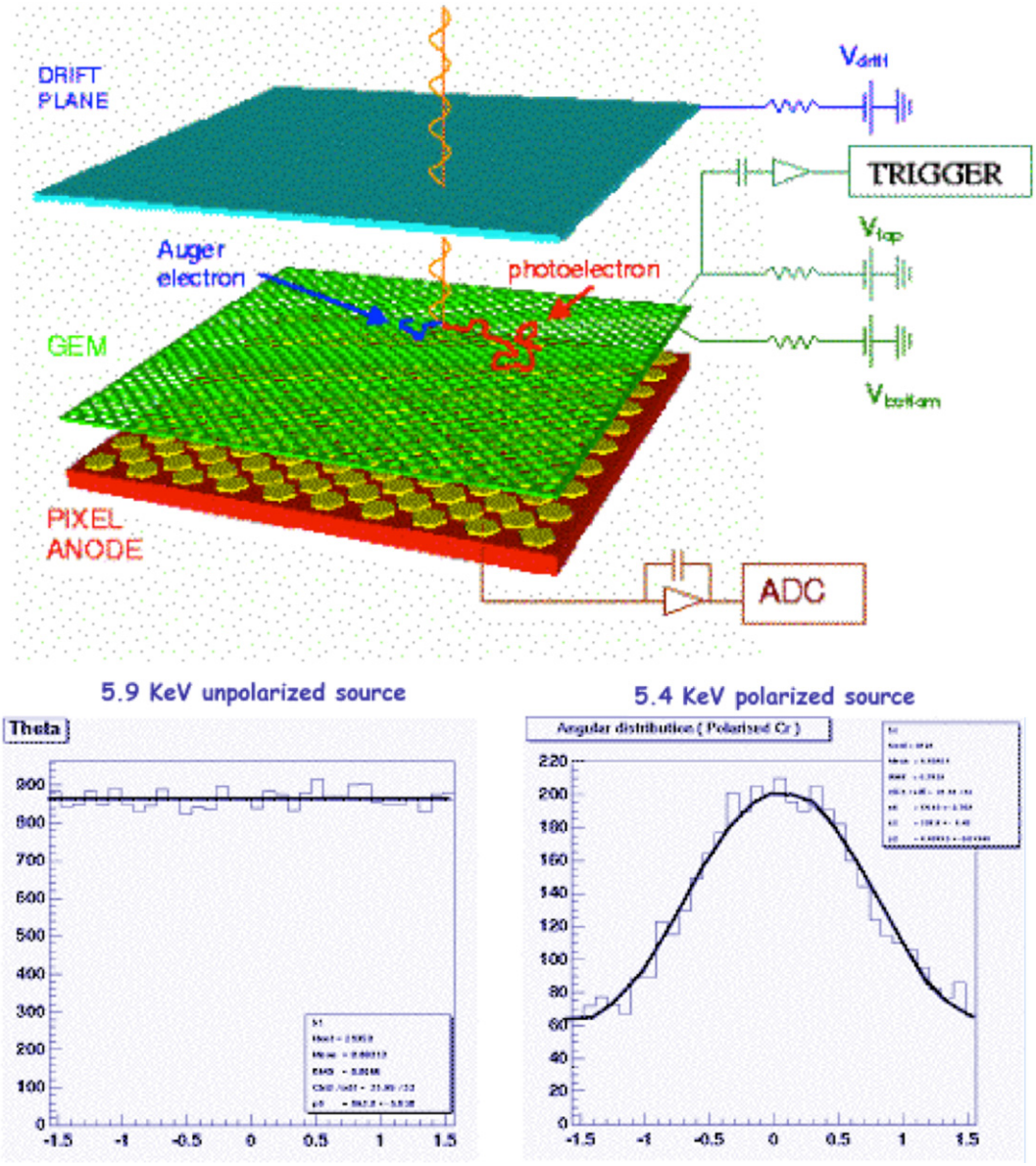

Fig. 66. Astrophysics application: detection of X-rays and the polarization.

(position, intensity profile, direction/emittance) is desired with a quick response faster than beam pulse period, in such a manner as to provide feedback information to correct small deviation from the planned therapeutic treatment.

9. Conclusions

In this review paper the present state-of-the-art of muon detection systems using gaseous detectors at the Large Hadron Collider (LHC) is described. Beginning with a discussion of the concepts of muon detection systems, a comparison of the various technologies used is made with respect to the challenges at present experiments and developments for future upgrades are discussed. Starting from wire chambers micropattern detectors are described and their readiness for upgrades is highlighted. Aging, long-term sustained operation and factors affecting gas choice are discussed. Finally some applications outside particle physics are also presented.

Acknowledgments

The author is indebted to Dr. M. Abbrescia, Dr. M. Maggi and Dr. D. Green for careful reading of the manuscript and giving valuable comments and suggestions. The Garfield simulations have been done by Y. Assran and I am grateful to S. Colafranceschi for the latex layout.

References

[1] L. Evans, P. Bryant, 2008 Journal of Instrumentation, 3 S08001.
[2] 〈http://www.linearcollider.org〉.
[3] F. Zimmermann, CERN, Geneva, Switzerland, LHC UPGRADE SCENARIOS 〈http://care-hhh.web.cern.ch/care-hhh/Literature/TUZAKI02n.pdf〉.
[4] F. Zimmermann, Accelerator Physics for ILC and CLIC, CERN, Geneva, Switzerland. 〈http://cdsweb.cern.ch/record/1269881/files/CERN-ATS-2010-056.pdf〉.
[5] M. Huhtinen, A. Rubbia, P.A. Aarnio, Nuclear Instruments and Methods in Physics Research Section A 351 (1994) 236.
[6] See review article on Particle Identification by C. Lippmann, doi:10.1016/j.nima.2011.03.009, this issue.

[7] See review article on Transition Radiation and Cenerkov Imaging by J. Wessels and A. Adronic, this issue. 〈http://www.sciencedirect.com/science/article/pii/S0168900211018134〉.
[8] K. Mitsui, Physical Review D 45 (1992) 3051.
[9] W.K. Sakumoto, et al., Physical Review D 45 (1992) 3042.
[10] G. Battistoni, et al., Nuclear Instruments and Methods in Physics Research Section A: Accelerators, Spectrometers, Detectors and Associated Equipment 394 (1–2) (1997) 136.
[11] See Review Paper on Magnet Systems by A. Gaddi, doi:10.1016/j.nima.2011.03.006, this issue.
[12] The ATLAS Experiment at the CERN Large Hadron Collider, Journal of Instrumentation, 19 3 (2008) S08003.
[13] CMS Collaboration, CMS experiment at the CERN LHC, Journal of Instrumentation 3 (2008) S08004.
[14] M. Huhtinen Radiation environment for the CMS detector, CERN CMS TN/95-198.
[15] S.F. Biagi, Nuclear Instruments and Methods in Physics Research A 421 (1999) 234.
[16] F. Barbosa, R. Dumps, J.S. Graulich, A. Kachtchouk, L. Manhaes, de A. Filho, E. Polycarpo, W. Riegler, B. Schmidt, T. Schneider, V. Souvorov, IEEE Transactions on Nuclear Science 53 (1) (2006).
[17] A. Sharma, in: Proceeding of the Conference MPGD2011, submitted.
[18] P. Gros, for the ALICE Collaboration, Acta Physica Polonica B 42 (7) (2011).
[19] The ATLAS TRT collaboration, Journal of Instrumentation 3 (February) (2008) P02014 doi:10.1088/1748-0221/3/02/P02014.
[20] P. Lichard, Journal of Instrumentation 5 (2010) C12053. 〈http://iopscience.iop.org/1748-0221/5/12/C12053〉.
[21] M.C.S. Williams, ALICE collaboration, Nuclear Physics A 661 (1–4) (1999) 707.
[22] R. Santonico, RPC: Status and perspectives, in: ∗Pavia 1993, Proceedings, The Resistive Plate Chambers in Particle Physics and Astrophysics, vol. 11, pp. 1–7.
[23] A. Blanco, et al., A Large-Area Timing RPC (2002) 〈www.slac.stanford.edu/pubs/icfa/fall01/paper1/paper1.pdf〉.
[24] L. Benussi, et al., Journal of Instrumentation 4 (2009) P08006 arXiv:0812.1710 [physics.ins-det].
[25] P. Antonioli, Nuclear Physics B—Proceedings Supplements 125 (September) (2003) 193.
[26] CERN Courier: ALICE revolutionizes TOF systems: 〈http://cerncourier.com/cws/article/cern/47490〉.
[27] P. Fonte, et al., IEEE Transactions on Nuclear Science 48 (5) (2001).
[28] E. Etzion, et al., The Certification of ATLAS Thin Gap Chambers Produced in Israel and China, TAUP 2787-04 15 November 2004, 〈http://atlas.web.cern.ch/Atlas/project/TGC/www/tgc.html〉.
[29] K. Nagai, Nuclear Instruments and Methods in Physics Research Section A: Accelerators, Spectrometers, Detectors and Associated Equipment 384 (1) (1996) 219 (BEAUTY '96).
[30] W. Riegler, et al., Nuclear Instruments and Methods in Physics Research Section A: Accelerators, Spectrometers, Detectors and Associated Equipment 443 (1) (2000) 156.
[31] C. Amelung, The European Physical Journal C - Particles and Fields 33 (2004) (Supplement 1), s999–s1001, doi:10.1140/epjcd/s2004-03-1794-6.
[32] 〈http://www.phys.ufl.edu/∼pakhotin/publications/nima-instr08.pdf〉.
[33] A. Oed, Nuclear Instruments and Methods in Physics Research Section A: Accelerators, Spectrometers, Detectors and Associated Equipment 263 (2–3) (1988) 351.
[34] F. Sauli, A. Sharma, Annual Review of Nuclear and Particle Science 49 (1999) 341.
[35] B. Ketzer, et al., For the COMPASS collaboration, IEEE Transactions on Nuclear Science 49 (2002) 2403.
[36] G. Anelli et al., TOTEM Collaboration, Journal of Instrumentation 3 (2008) S08007. 〈http://iopscience.iop.org/1748-0221/3/08/S08007〉.
[37] M. Alfonsi, et al., The LHCb Triple-GEM Detector for the Inner Region of the First Station of the Muon System: Construction and Module-0 Performance 0-7803-8700-7/04 (C) 2004 IEEE.
[38] A. Bressan, A. Buzulutskov, L. Ropelewski, F. Sauli, L. Shekhtman, Nuclear Instruments and Methods in Physics Research Section A 432 (1999) 119.
[39] Y. Bilevych, et al., Nuclear Physics B—Proceedings Supplements 215 (1) (2011) 51–55.
[40] Y. Giomataris, et al., Nuclear Instruments and Methods in Physics Research Section A 376 (1996) 29.
[41] J. Wotchak, in: Proceedings of the conference MPGD 2011, submitted.
[42] A. Sharma, ICFA Bulletin Fall 1999 〈http://www.slac.stanford.edu/pubs/icfa〉.
[43] D. Abbaneo, et al., Construction of the First Full-Size GEM-Based Prototype for the CMS High-η Muon System, 2010 IEEE, doi:10.1109/NSSMIC.2010.5874107.
[44] D. Abbaneo, et al., Characterization of GEM Detectors for Application in the CMS Muon Detection System, 2010 IEEE Proceeding, doi:10.1109/NSSMIC.2010.5874006.
[45] J. Wiechula and the ALICE TPC Collaboration, Commissioning and Calibration of the ALICE TPC, doi:10.1016/j.nuclphysa.2009.10.046.
[46] S. Dorheim, TPC Readout with GEMs for the ILC MPGD 2011, submitted.
[47] B. Yu, et al., A GEM Based TPC for the LEGS Experiment, 2005 IEEE Nuclear Science Symposium Conference Record.
[48] M. Capeans, Nuclear Instruments and Methods in Physics Research Section A: Accelerators, Spectrometers, Detectors and Associated Equipment 515 (1–2) (2003) 73.
[49] C. Niebuhr, Nuclear Instruments and Methods in Physics Research Section A: Accelerators, Spectrometers, Detectors and Associated Equipment 566 (1) (2006) 118 DESY, Notkestr. 85, 22607 Hamburg, Germany.
[50] M. Titov, M. Hohlmann, C. Padilla, N. Tesch, Summary and Outlook of the International Workshop on Aging Phenomena in Gaseous Detectors, DESY, Hamburg, October 2001).
[51] G. Aielli, et al., IEEE Transactions on Nuclear Science 53 (2) (2006) 567.
[52] A. Sharma, Summary of RPC 2007, the IX International Workshop on Resistive Plate Chambers, in: Proceedings of NIMA, 2009.
[53] M. Abbrescia, HF Production in CMS-Resistive Plate Chambers, doi:10.1016/j.nuclphysbps.2006.07.002.
[54] M. Alfonsi, et al., IEEE Transactions on Nuclear Science 53 (1) (2006).
[55] Y. Assran, A. Sharma, Transport Properties of Operational Gas Mixtures Used at LHC, arxiv.org/pdf/1110.6761.
[56] R&D on Calorimetry for the ILC Inside the CALICE Collaboration.
[57] Jose' Repond, Construction of a Digital Hadron Calorimeter, for the DHCAL Collaboration, arXiv:1005.0410v1.
[58] J. Yu, et al., Application of large scale GEM for digital Hadron calorimetry, in: Proceedings of MPGD2011, to be published.
[59] R. Chechik, A. Breskin, C. Shalem, Review of Scientific Instruments 74 (2003) 2148. doi:10.1063/1.1537873. 〈http://arxiv.org/ftp/physics/papers/0502/0502131.pdf〉.
[60] D. Pacella, et al., Review of Scientific Instruments 74 (2003) 2148. doi:10.1063/1.1537873.
[61] A. Blanco, et al., IEEE Transaction on Nuclear Science 53 (5) (2006) 2489.
[62] M. Hohlmann, et al., Design and Construction of a First Prototype Muon Tomography System with GEM Detectors for the Detection of Nuclear Contraband, 〈http://arxiv.org/ftp/arxiv/papers/0911/0911.3203.pdf〉.
[63] R. Bellazini, et al., IEEE Transactions on Nuclear Science 49 (3) (2000).